Bulletin of Volcanology

Understanding the drivers of volcano deformation through geodetic model verification and validation

--Manuscript Draft--

Manuscript Number:	
Full Title:	Understanding the drivers of volcano deformation through geodetic model verification and validation
Article Type:	Research Article
Corresponding Author:	Josh Crozier, Ph.D. United States Geological Survey Moffett Field, California UNITED STATES
Corresponding Author Secondary Information:	
Order of Authors:	Josh Crozier, Ph.D.
	Leif Karlstrom
	Emily Montgomery-Brown
	Mario Angarita
	Valérie Cayol
	Mary-Grace Bato
	Taiyi A Wang
	Ronni Grapenthin
	Tara Shreve
	Kyle R Anderson
	Ana Astort
	Olivier Bodart
	Flavio Cannavó
	Gilda Currenti
	Farshid Dabaghi
	Brittany Erickson
	Deepak Garg
	Matthew Head
	Adriana Iozzia
	Young Cheol Kim
	Hélène Le Mével
	Camila Novoa Lizama
	Cody Rocker
	Francesca Silverii
	Elisa Trasatti
	Yan Zhan
Funding Information:	National Science Foundation (EAR1830873) — Not applicable
	National Science Foundation

	(EAR1824343)	Not applicable
	European Research Council (866085)	Dr. Camila Novoa Lizama
	Istituto Nazionale di Geofisica e Vulcanologia (1865)	Dr. Ana Astort Dr. Elisa Trasatti
	European Research Council (101017501)	Dr. Francesca Silverii
	National Science Foundation (1848554)	Dr. Leif Karlstrom
	National Science Foundation (2019232)	Dr. Ronni Grapenthin
	National Science Foundation (1855125)	Mr. Mario Angarita

Abstract:	Volcano geodesy involves using models to explain observed surface deformation. A wide variety of forward models are used, from analytical point sources to numerical simulations that consider complex source geometries, topography, and material properties. A wide variety of inverse methods are then used to relate models to data. Ideally, forward models should be verified through intercomparison, and inverse methods should be validated through tests with synthetic and/or real data. However, to date there have not been comprehensive verification and validation efforts in volcano geodesy. Here, we report on the first phase of the Drivers of Volcano Deformation (DVD) verification and validation exercises, which were designed to build community involvement through web-based exercises involving static elastic displacement around pressurized magma reservoirs. The forward model exercises began with a spherical reservoir in a homogeneous half space, then introduced topography, heterogeneous elastic properties, and spheroidal geometries. The inversion exercises provided synthetic noisy surface displacement data for a spherical reservoir in a homogeneous half space and assess consistency in estimates of reservoir location and volume/pressure change. There is appreciable variability in both forward model and inversion submissions which highlights the strengths and limitations of different forward models, as well as the importance of using accurate inverse methods and uncertainty quantification. This first phase of the DVD exercises serves as a community resource and will facilitate future developments towards establishing standards of reproducibility.

Suggested Reviewers:	Timothy Masterlark Professor, South Dakota School of Mines and Technology timothy.masterlark@sdsmt.edu
	James Hickey Senior Lecturer, University of Exeter J.Hickey@exeter.ac.uk
	Mehdi Nikkhoo Postdoc, Helmholtz-Zentrum Potsdam GFZ: Deutsches Geoforschungszentrum Potsdam mehdi.nikkhoo@gfz-potsdam.de
	Jeff Freymueller Professor, Michigan State University freymuel@msu.edu
	Pablo Gonzalez Researcher, Instituto de Productos Naturales y Agrobiologia pabloj.gonzalez@csic.es
	Aline Peltier Institut de Physique du Globe de Paris peltier@ipgp.fr
Author Comments:	

Understanding the drivers of volcano deformation through geodetic model verification and validation

Josh Crozier, Leif Karlstrom, Emily Montgomery-Brown, Mario Angarita, Valérie Cayol, Mary Grace Bato, Taiyi A. Wang, Ronni Grapenthin, Tara Shreve, Kyle Anderson, Ana Astort, Olivier Bodart, Flavio Cannavò, Gilda Currenti, Farshid Dabaghi, Brittany A. Erickson, Deepak Garg, Matthew Head, Adriana Iozzia, Young Cheol Kim, Hélène Le Mével, Camila Novoa Lizama, Cody Rucker, Francesca Silverii, Elisa Trasatti, Yan Zhan

1. Josh Crozier
    a. jcrozier@usgs.gov
    b. 0000-0001-8996-3441
    c. U.S. Geological Survey California Volcano Observatory, Moffett Field, CA, USA
2. Leif Karlstrom
    a. leif@uoregon.edu
    b. 0000-0002-2197-2349
    c. University of Oregon, Eugene, OR
3. Emily Montgomery-Brown
    a. emontgomery-brown@usgs.gov
    b. 0000-0001-6787-2055
    c. U.S. Geological Survey Cascades Volcano Observatory, Vancouver WA, USA
4. Mario Angarita
    a. mfangaritasr@alaska.edu
    b. 0000-0001-7455-2455
    c. University of Alaska Fairbanks, Fairbanks, AK, USA
5. Valérie Cayol
    a. valerie.cayol@uca.fr
    b. 0000-0001-9225-7441
    c. Université Clermont Auvergne, Clermont-Ferrand, France
6. Mary-Grace Bato
    a. bato@jpl.nasa.gov
    b. 0000-0002-8390-1087
    c. NASA JPL, Pasadena, CA, USA
7. Taiyi A. Wang
    a. taiyi@stanford.edu
    b. 0000-0002-5933-6866
    c. Stanford University, Stanford, CA, USA
8. Ronni Grapenthin
    a. rgrapenthin@alaska.edu
    b. 0000-0002-4926-2162
    c. University of Alaska Fairbanks, Fairbanks, AK, USA
9. Tara Shreve
    a. tshreve@carnegiescience.edu
    b. 0000-0003-2103-2434
    c. Carnegie Institution for Science, Washington, DC, USA; Now at University of Alaska Fairbanks, Fairbanks, AK, USA
10. Kyle R. Anderson
    a. kranderson@usgs.gov
    b. 0000-0001-8041-3996
    c. U.S. Geological Survey California Volcano Observatory, Moffett Field, CA, USA

11. Ana Astort
    a. ana.astort@ingv.it
    b. 0000-0001-6560-249X
    c. Istituto Nazionale di Geofisica e Vulcanologia, Rome, Italy
12. Olivier Bodart
    a. olivier.bodart@univ-st-etienne.fr
    b. 0000-0001-9341-7283
    c. Université Jean Monnet Saint-Etienne: Saint-Etienne, Rhône-Alpes, France
13. Flavio Cannavò
    a. flavio.cannavo@ingv.it
    b. 0000-0001-7550-8579
    c. Istituto Nazionale di Geofisica e Vulcanologia, Catania, Italy
14. Gilda Currenti
    a. gilda.currenti@ingv.it
    b. 0000-0001-8650-5613
    c. Istituto Nazionale di Geofisica e Vulcanologia, Sezione di Catania, Italy
15. Farshid Dabaghi
    a. farshid.dabaghi@univ-st-etienne.fr
    b. 0000-0001-5824-3839
    c. Institut Camille Jordan, Université Jean Monnet, Saint-Etienne, France
16. Brittany A. Erickson
    a. bae@uoregon.edu
    b. 0000-0001-9457-8572
    c. University of Oregon, Eugene, OR, USA
17. Deepak Garg
    a. deepak.garg@ingv.it
    b. 0000-0003-2463-5185
    c. Istituto Nazionale di Geofisica e Vulcanologia, Pisa, Italy
18. Matthew Head
    a. mshead@illinois.edu
    b. 0000-0003-0103-8329
    c. University of Illinois at Urbana-Champaign, Urbana, IL, USA
19. Adriana Iozzia
    a. adriana.iozzia@phd.unict.it; adriana.iozzia@ingv.it
    b. 0000-0001-9912-4422
    c. Università degli Studi di Catania, Catania, Italy; Istituto Nazionale di Geofisica e Vulcanologia, Sezione di Catania, Italy
20. Young Cheol Kim
    a. yvk5286@psu.edu
    b. 0000-0003-2401-9059
    c. Pennsylvania State University, State College, PA, USA
21. Hélène Le Mével
    a. hlemevel@carnegiescience.edu
    b. 0000-0002-6257-9885
    c. Carnegie Institution for Science, Washington, DC, USA
22. Camila Novoa Lizama
    a. c.p.novoalizama@leeds.ac.uk
    b.
    c. School of Earth and Environment, University of Leeds, Leeds, UK

23. Cody Rucker
    a. crucker@uoregon.edu
    b. 0000-0002-7418-0185
    c. University of Oregon, Eugene, OR, USA
24. Francesca Silverii
    a. francesca.silverii@ingv.it
    b. 0000-0002-7039-5875
    c. Istituto Nazionale di Geofisica e Vulcanologia, Rome, Italy
25. Elisa Trasatti
    a. elisa.trasatti@ingv.it
    b. 0000-0002-2983-045X
    c. Istituto Nazionale di Geofisica e Vulcanologia, Rome, Italy
26. Yan Zhan
    a. yanzhan@cuhk.edu.hk
    b. 0000-0002-2623-3238
    c. The Chinese University of Hong Kong, Hong Kong

Author Contributions

Original draft: Josh Crozier

Review and editing: Leif Karlstrom, Valérie Cayol, Ronni Grapenthin, Kyle Anderson, Tara Shreve, Taiyi Wang, Camila Novoa, Gilda Currenti, Elisa Trasatti

Exercise planning and design: Leif Karlstrom, Emily Montgomery-Brown, Josh Crozier, Valérie Cayol, Mary-Grace Bato, Ronni Grapenthin

Website design: Mario Angarita Vargas

Exercise participation: Josh Crozier, Leif Karlstrom, Mario Angarita, Valérie Cayol, Taiyi A. Wang, Tara Shreve, Kyle Anderson, Ana Astort, Olivier Bodart, Flavio Cannavò, Gilda Currenti, Farshid Dabaghi, Brittany A. Erickson, Deepak Garg, Matthew Head, Adriana Iozzia, Young Cheol Kim, Hélène Le Mével, Camila Novoa Lizama, Cody Rucker, Francesca Silverii, Elisa Trasatti, Yan Zhan

Additional analysis: Josh Crozier, Leif Karlstrom, Taiyi Wang, Tara Shreve, Valérie Cayol, Kyle Anderson

Competing Interests:

The authors declare that no competing interests are present

Acknowledgements

Support was provided by the U.S. National Science Foundation (NSF) Research Coordination Network (RCN): Community Network for Volcanic Eruption Response (CONVERSE) under award NSF-EAR1830873 and Modeling Collaboratory for Subduction under award NSF-EAR1824343. Support was also provided by the International Association of Volcanology and Chemistry of the Earth's Interior (IAVCEI) Commission on Volcano Geodesy. CNL acknowledges support from the European Research Council (ERC) through the EU Horizon 2020 project DEEPVOLC (Grant 866085). AA and ET acknowledge funding by the LOVE-CF project 2020-2023 (INGV, Internal Register no. 1865 17/07/2020). FS acknowledges support by the EU Horizon 2020 project RELIANCE (Grant 101017501). LK acknowledges support from NSF grant 1848554. RG acknowledges support from NSF grant 2019232. MA acknowledges partial support through NSF grant 1855126. The exercise website can be found at www.driversofvolcanodeformation.org, and plotting scripts can be found in the supplement or at https://bitbucket.org/crozierjosh1/dvd/src/. Any use of trade, firm, or product names is for descriptive purposes only and does not imply endorsement by the U.S. government.

Abstract

Volcano geodesy involves using models to explain observed surface deformation. A wide variety of forward models are used, from analytical point sources to numerical simulations that consider complex source geometries, topography, and material properties. A wide variety of inverse methods are then used to relate models to data. Ideally, forward models should be verified through intercomparison, and inverse methods should be validated through tests with synthetic and/or real data. However, to date there have not been comprehensive verification and validation efforts in volcano geodesy. Here, we report on the first phase of the Drivers of Volcano Deformation (DVD) verification and validation exercises, which were designed to build community involvement through web-based exercises involving static elastic displacement around pressurized magma reservoirs. The forward model exercises began with a spherical reservoir in a homogeneous half space, then introduced topography, heterogeneous elastic properties, and spheroidal geometries. The inversion exercises provided synthetic noisy surface displacement data for a spherical reservoir in a homogeneous half space and assess consistency in estimates of reservoir location and volume/pressure change. There is appreciable variability in both forward model and inversion submissions which highlights the strengths and limitations of different forward models, as well as the importance of using accurate inverse methods and uncertainty quantification. This first phase of the DVD exercises serves as a community resource and will facilitate future developments towards establishing standards of reproducibility.

Keywords: Volcano Geodesy, Volcano Deformation, Validation and Verification, Modelling

Statements and Declarations: The authors declare that no competing interests are present.

1. Introduction

Over 200 volcanoes around the world are known to be actively exhibiting ground deformation (Ebmeier et al., 2018). This number will continue to rise from expansion of ground-based monitoring networks, increases in the amount and types of satellite imagery available, and improvements in data processing and analysis methods (Poland and Zebker, 2022). Activity over timescales not captured in previous data will also substantially contribute to increasing the number of known actively deforming volcanoes (Grapenthin et al., 2022).

Ground deformation in volcanic settings can arise from a variety of causes. Deformation can reflect pressurizing/depressurizing subsurface magma bodies, which could have geometries ranging from spheroid-like fluid-filled reservoirs to complex networks of dikes, sills, and crystal mush regions (Bato et al., 2021; Ebmeier et al., 2018; Grapenthin et al., 2022; Montgomery-Brown and Miklius, 2021; Mullet and Segall, 2022). Deformation can also reflect processes such as flank slip or other volcanic/tectonic faulting (Dumont et al., 2022; Poland et al., 2017) and hydrothermal activity (Fournier and Chardot, 2012). Having accurate forward models of deformation from these various processes is important for resolving magma storage geometries and understanding stress states that influence flank stability (Gonzalez-Santana and Wauthier, 2021), eruption triggering (Gregg et al., 2013), dike trajectories (Karlstrom et al., 2009; Sigmundsson et al., 2015), caldera collapse onset and expected eruptive volumes (Anderson et al., 2019; Sigmundsson et al., 2020), and overall eruptive cycles (Townsend, 2022). To resolve these processes and detect signs of unrest, it is important to be able to relate deformation models to monitoring data (Fernández et al., 2017).

There are a wide variety of different forward models and inverse methods in use for studying volcano deformation. Comparisons between particular models have been made previously (Battaglia et al., 2013; Hickey and Gottsmann, 2014; Novoa et al., 2019; Segall, 2010; Taylor et al., 2021), but there has not yet been a comprehensive community wide model and inversion intercomparison initiative. Such initiatives for earthquake science have been carried out over the last two decades by the Southern California

Earthquake Center (SCEC), including for both the Spontaneous Rupture Code Verification and simulations of Sequences of Earthquake and Aseismic Slip (SEAS) projects, (Barall and Harris, 2015; Erickson et al., 2020; Harris et al., 2018, 2011, 2009; Jiang et al., 2022; Mai et al., 2016), which have been influential for establishing standards of reproducibility and driving new methods development. We follow this blueprint to introduce an initial phase of volcano deformation community exercises. The exercises include both verification, or testing that forward models are implemented accurately, and validation, or testing that models agree with reality (of which these exercises consider only the initial step of testing inversions against synthetic data) (Gonnermann and Anderson, 2021).

The exercises carried out in this work were inspired by the success of SCEC exercises, which over time have developed into a multi-pronged community initiative that now helps push the boundaries of earthquake and fault mechanics modeling. A steering committee (Karlstrom, Montgomery-Brown, Crozier, Bato, Cayol) was formed in fall 2021 in partnership with CONVERSE, MCS-RCN (Gonnermann and Anderson, 2021), and the IAVCEI volcano geodesy commission (no financial support). An initial virtual planning workshop was advertised to the community and held in October 2021 with 32 attendees. The steering committee then used community suggestions to finalize the exercise design, and hired a student (Angarita) to develop a website (www.driversofvolcanodeformation.org, Fig. 1) which provides complete problem specifications and the ability to download or interactively plot and compare submitted solutions. The website was published in February 2022. The exercises were advertised through email listservs (ASU Volcano Digest, IAVCEI Geodesy Commission, SZ4D Modeling Collaboratory for Subduction) and presentations/meetings at multiple conferences: AGU (Montgomery-Brown et al., 2022), EGU, Cities on Volcanoes, and IUGG (Cayol et al., 2023). Virtual office hours for participants were held in various time zones. Twenty-six researchers from multiple continents and career stages participated, and the website is intended to remain open for continuing submissions so that it can serve as a general resource for method selection, verification, and validation. In summer 2023 results were compiled and participants were asked to provide feedback. This article outlines the exercises, presents key results, and discusses future initiatives.

2. Forward model (verification) exercises

We kept the scope of this first phase of exercises limited by focusing on static elastic displacement, which is a necessary step for community consistency before considering more complex and time-dependent modeling (e.g., thermo-poro-visco-elasticity of host rocks or treatment of multiphase magma dynamics) and inversions (e.g., time-series data processing methods or sensor network design). We also focused on inflating/deflating spheroidal magma reservoirs, which are the most common sources used in both inversions and general magma reservoir models. Since there are limits to how uniquely complex source geometries and rheology can be resolved (Segall, 2019), linear elastic spheroidal reservoir models will remain valuable and widely used even as more sophisticated methods continue to be developed.

For forward modeling of elastic spheroidal reservoirs, a wide variety of both analytical and numerical methods are in use. Analytical models are widely used due to their simplicity and low computational cost, which is beneficial for inversions (Lisowski, 2006; Taylor et al., 2021). Most analytical models assume a homogeneous elastic half space (McTigue, 1987; Mogi, 1958; Yang et al., 1988), and are approximations that become less accurate for small depth/radius ratios and/or eccentricities. A recently derived series expansion solution for a spherical reservoir can be arbitrarily accurate but at greater computational cost (Zhong et al., 2019). Several approximate corrections for topography with varying computational cost and accuracy can be used with analytical models (McTigue and Segall, 1988; Williams and Wadge, 2000). There are multiple different implementations in use for many of the analytical models and corrections, and implementation errors have previously been found in some published versions.

Numerical models can be more general than analytical models (Masterlark, 2007), but also typically

involve higher computational cost and have accuracy that depends upon user choices about factors such as mesh resolution and domain size. Volume discretized approaches such as finite element methods (FEMs) are robust and general, and many different types of FEMs are commonly used in volcano geodesy. FEMs are sensitive to choices of domain size and boundary conditions, as well as choice of interpolation functions and mesh generation (Novoa et al., 2019; Zienkiewicz, 2005). Some widely used FEMs are commercial, although open source options are also available (Aagaard et al., 2013; Bodart et al., 2022; Garg et al., 2021; Lindsay et al., 2022; Longo et al., 2012; Rucker et al., 2022). Boundary integral or boundary element methods (BEMs) only discretize boundaries where stress or displacement conditions are applied, and several types are used (Cayol and Cornet, 1997; Crouch and Starfield, 1983). BEMs produce denser system matrices than FEMs, but typically have fewer degrees of freedom and thus are often more computationally efficient. BEMs also typically require fewer user choices than FEMs. However, BEMs are generally limited to homogeneous materials, and the commonly used constant dislocation BEM only converges within a few percent without additional treatment of dislocation edge singularities (Liu, 2016). Other numerical approaches such as finite difference (Coco et al., 2014) or finite volume methods are at present less commonly used for volcano deformation, but are common in the similar problems associated with fault mechanics (Erickson et al., 2020).

We present a series of verification exercises. In each exercise participants used models of their choice to submit predictions of displacements and stresses along two 5 km long radial transects: a surface transect and a subsurface transect halfway between the top of the reservoir and the surface. We asked participants to provide metadata about mesh resolution, domain size, and domain boundary condition, but we did not provide guidelines on these choices or on convergence testing in order to gain a sense for the accuracy of models as they are used in practice. Solutions could be submitted following the format specifications given on the community website in either “guest” mode for testing, and as permanent submissions linked to a user account (which could be updated at later times by the submitter).

All problems solve the equations of static linear elasticity without a body force (no gravity)

$$\frac{\partial \sigma_{ij}}{\partial x_j} = 0 \qquad 1.$$

along with appropriate boundary and standard compatibility conditions. σ_{ij} is the stress tensor (using ‘Einstein’ notation in which repeated indices are summed) in an isotropic (although possibly inhomogeneous) linear elastic solid following Hooke's law

$$\sigma_{ij} = \lambda e_{kk}\delta_{ij} + 2G e_{ij} \qquad 2.$$

where e_{ij} is the strain tensor (repeated indices are summed), δ_{ij} is the delta function and λ and G are elastic constants (Lamé parameters) that may be spatially variable in inhomogeneous scenarios. Hooke's law is often written in terms of Poisson's ratio $\nu = \lambda/(2(\lambda + G))$ and Young's Modulus $E = 2G/(1+\nu)$ as $Ee_{ij} = (1+\nu)\sigma_{ij} - \sigma_{kk}\delta_{ij}$.

We present all forward models by showing the normalized root mean squared difference (NRMSD) of each solution component (displacement or stress) s_i from reference solution component s_i^{ref}:

$$NRMSD_i = \left(\sum_{n=1}^{N} \left(s_i(n) - s_i^{ref}(n)\right)^2\right)^{1/2} \left(\sum_{n=1}^{N} \left(s_i^{ref}(n)\right)^2\right)^{-1/2} \qquad 3.$$

for N points along the radial transects. For exercises without surface topography, shear stress components of surface transects should be zero to satisfy the free surface condition. For these components we instead use:

$$NRMSD_i = \frac{1}{PN^{1/2}}\left(\sum_{n=0}^{N} (s_i(n))^2\right)^{1/2} \quad 4.$$

where the prescribed pressure P is included to nondimensionalize the error expression. For exercises where an exact analytical solution is known, we use this as the reference solution so that the NRMSD metric directly measures error. For exercises where an exact analytical solution is not known, we use a mean of other solutions as the reference solution so that the NRMSD metric provides information about the variation between solutions. The NRMSD metric provides a compact way to examine model accuracy or variance, but it does not reveal the spatial distribution of model error/variance. We thus also plot surface displacements for all exercises, and more detail can be seen in the full solution plots in supplemental figures S1-S12.

2.1. Forward model exercise 1: sphere in a homogeneous half space

Exercise 1 considers a spherical reservoir at three different depths in a homogeneous half space (Fig. 2); this serves as a benchmark since an analytic series expansion that converges to the exact solution can be computed (Zhong et al., 2019). We ask participants to solve the quasistatic linear elastic governing equations on a semi-infinite Cartesian (x, y, z) domain with coordinate origin centered on a flat stress-free interface above a spherical magma reservoir surface Ω defined by $x^2 + y^2 + (z + D)^2 = R^2$ with reservoir radius R = 1 km and reservoir centroid depth below the free surface D. With the domain defined, boundary conditions for Cauchy and Hooke equations are

$$\sigma_{ij}(\Omega)n_j n_i = -P$$
$$\sigma_{zz}(x, y, z = 0) = 0$$
$$\sigma_{rz}(x, y, z = 0) = 0 \quad 5.$$

with n an inward pointing normal vector, and P the chamber pressure change (relative to lithostatic pressure). It is understood that traction goes to zero far from the chamber in the half space. Exercises 1A, 1B, and 1C use reservoir centroid depth D of 1.25 km, 2 km, and 4 km, respectively. All three scenarios use uniform ν = 0.25, G = 10 GPa, and P = 10 MPa.

Multiple analytical approximations/solutions are available for exercise 1. We use the series expansion solution of (Zhong et al., 2019) calculated to 64th order, which testing shows converges to near machine precision for the source depth/radius ratios considered in these exercises, as the reference solution for comparing other solutions against (Fig. 2, 3, 4, and 5). We note that these exercises identified an error in the published implementation of this solution. Figure 3 shows the convergence of the commonly used Mogi and McTigue models with increasing depth (i.e., depth/radius ratio), illustrating convergence of NRMSD at near-expected rates ($(R/D)^3$ for Mogi and $(R/D)^6$ for McTigue). Implementation errors were also fixed in the dModels and VSM McTigue solutions as a result of these exercises (Battaglia et al., 2013; Trasatti, 2022), although there is still some difference between the McTigue submissions in these exercises. However, as expected, all of the McTigue models become more accurate with increasing source depth (i.e., source depth/radius ratio). For the 1.25 km deep source Mogi and McTigue models show significant surface displacement error (0.47 NRMSD for Mogi and 0.23 NRMSD for McTigue, Fig. 4), for the 2 km deep source the Mogi model still shows significant error (0.11 NRMSD) but the McTigue models are reasonably accurate (0.01 NRMSD), and for the 4 km deep source both types of models are reasonably accurate (NRMSD <~0.01). Stresses are generally inaccurate for these models (NRMSD ~1). All of the analytical solutions have computation times <<1 s, except for the series expansion solution of (Zhong et al., 2019) which can take multiple seconds if many terms (>50) in the infinite series expansion are computed.

Several 3D BEM solutions were submitted. Two dislocation BEMs using the triangular element of (Nikkhoo and Walter, 2015) were submitted with different numbers of source mesh elements (320 and

4972). Both show similar surface displacement accuracy to the McTigue models (up to 0.21 NRMSD) for the 1.25 km deep source, but their accuracy does not increase as quickly with depth. The dislocation BEMs provide generally more accurate stresses than McTigue models, but still exhibit up to 1 NRMSD for subsurface zz components. Convergence testing for a constant dislocation BEM demonstrates that it does not actually converge as the mesh is refined (Fig. 5) due to element edge singularity effects. A mixed BEM (MBEM) (Cayol and Cornet, 1997) was submitted with up to 5120 source mesh elements; this provides reasonably accurate stresses and displacements for all depths (<0.05 NRMSD) and converges with source mesh refinement (Fig. 5). The BEMs have reported computation times of tens of seconds to tens of minutes per simulation, appreciably longer than all of the analytical models.

Multiple FEM solutions were submitted; some with commercial software COMSOL® and Marc®, and others with open-source codes or libraries: PyLith (Aagaard et al., 2013), GALES (Garg et al., 2021; Longo et al., 2012), MOOSE (Lindsay et al., 2022), NGSOLVE (Rucker et al., 2022), and DEFVOLC fictitious domain based on getFEM++ (Bodart et al., 2022, 2020). All of the FEM solutions have <0.1 NRMSD in displacements and stresses for all source depths. Some outlier FEM solutions are 3D, so likely used coarser meshes for computational reasons. We show convergence testing from two models: NGSOLVE using 4th order elements and COMSOL® using 2nd order elements (Fig. 5). We do not address factors such as mesh size and element order in detail, but note that for quadratic elements even a fairly coarse mesh size of 270 m can yield error < 0.01 NRMSD given a large enough domain size. However, domain sizes of 20 km (or 10 times the reservoir depth) are needed to obtain error < 0.01 NRMSD, whether “fixed” (zero displacement) or “roller” (zero normal displacement plus zero tangential traction) domain edge boundary conditions are used. In contrast, the “infinite element” coordinate transform approach enables high accuracy to be achieved with a domain size only slightly larger than the region of interest. Reported computation times vary from several seconds to several minutes per simulation for 2D models, and tens of minutes for 3D models. Computation times for the 2D models would generally increase by at least around two orders of magnitude when moving to 3D, suggesting that 3D computation times for most of the FEMs would be slower than the 3D BEMs.

One solution was submitted using a Gaussian process emulator trained on around 500 FEM simulations (Anderson and Gu, 2023; Anderson et al., 2019). This model has accuracy similar to the best FEM solutions for surface displacements for all scenarios. Computation times per emulator call are on the order of 0.001 s, which is comparable to most analytical models, although this does not consider time required to train the emulator.

2.2. Forward model exercise 2A: sphere in a homogeneous half space with topography

Exercise 2A considers a spherical reservoir in a homogeneous half space overlain by surface topography consisting of a Gaussian “volcano” (Fig. 6). The setup is the same as exercise 1B, but with boundary conditions given by

$$\sigma_{ij}(\Omega)n_j n_i = -P$$
$$\sigma_{zz}(x, y, z = h(\rho)) = 0$$
$$\sigma_{rz}(x, y, z = h(\rho)) = 0 \quad (6.)$$

Where $\rho = x^2 + y^2$ is a 2D (cylindrical) distance and

$$h(\rho) = Hexp\left(-\frac{\rho^2}{2R_e^2}\right) \quad (7.)$$

defines a Gaussian volcanic edifice overlying the magma chamber. Parameters are R = 1 km, D = 2 km (beneath the flat surface), R_e = 1 km, H = 1.5 km, ν = 0.25, G = 10 GPa and P = 10 MPa.

In exercise 2A, exact solutions are not known so we use the average of all submitted FEM solutions as a

reference solution to examine the variance in model results, after verifying that there are no visibly large outliers in the individual FEM solutions (Fig. 6, 7). In this exercise analytical models that neglect topography or only apply a varying depth (zeroth-order) correction (Williams and Wadge, 1998) produce appreciably different surface displacements (by at least 0.2 NRMSD) from numerical models, highlighting the importance of accounting for topography in this scenario. Two existing implementations of the Williams & Wadge (2000) small slope (first-order) topographic corrections produce different surface displacements from each other, and also differ from numerical models. This suggests that there is an error in at least one of the implementations, but it also highlights the limits of the correction for large topography. The first-order corrections require computation times of seconds for a McTigue model, so could be faster than numerical models and thus useful for smaller topography. Variance in all numerical (FEM + MBEM) solutions is less than 0.03 NRMSD for displacements and 0.07 NRMSD for stress, and some of the outlier FEM solutions are 3D and thus likely used coarser meshes to reduce computational cost.

2.3. Forward model exercise 2B: spheroid in a homogeneous half space

Exercise 2B considers an oblate (vertically shortened) sill-like spheroidal reservoir in a homogeneous half space (Fig. 8). The setup is the same as exercise 1, but with chamber defined by

$$\frac{\rho^2}{R_\rho^2} + \frac{z^2}{R_z^2} = 1 \qquad 8.$$

Parameters are R_p = 1 km, R_z = 0.1 km, D = 1.1 km, ν = 0.25, G = 10 GPa, and P = 10 MPa.

In exercise 2B, exact solutions are not known so we use the average of all submitted FEM solutions as a reference solution to examine the variance in model results, after verifying that there are no visibly large outliers (Fig. 8, 9). We show several approximate analytical models. The finite ellipsoidal model of (Cervelli, 2013) is extended from a previous model (Yang et al., 1988) and handles prolate or oblate dipping ellipsoids with accuracy that increases with the ratio of the shallowest depth along the spheroid over the minimum semi-diameter. The finite spheroidal model of (Nikkhoo and Rivalta, 2022) can consider more general geometries and predicts nearly identical displacements to (Cervelli, 2013), but requires more computation time (order 0.1 seconds compared to 0.01 seconds). Both of these models differ appreciably from FEM solutions (by 0.22 NRMSD) in this scenario. The point spheroid model of (Nikkhoo et al., 2017) is less accurate, differing from FEM solutions by 0.46 NRMSD. Another approximate analytical model for an ellipsoidal reservoir has been derived (Amoruso and Crescentini, 2013, 2011) but is not publicly available. We also show the analytical model for a penny-shaped crack of (Fialko et al., 2001), which for this highly oblate reservoir provides a reasonable approximation, differing from FEM solutions by 0.33 NRMSD.

The dislocation BEMs and the MBEM are similar to FEM results (within 0.10 NRMSD). Variance in all FEM solutions is less than 0.03 NRMSD, and some outlier FEM solutions are 3D and thus likely used coarser meshes for computational reasons.

2.4. Forward model exercise 2C: sphere in a heterogeneous half space

Exercise 2C considers a spherical reservoir in a heterogeneous half space where elastic moduli vary with distance from the reservoir to approximate a thermal gradient (Fig. 10). The setup is the same as exercise 1B, but with spatially variable elastic coefficients. Poisson's ratio and Young's modulus are assumed to be temperature dependent following (Bakker et al., 2016) and vary in a radial direction away from the chamber, with $r^2 = x^2 + y^2 + (z + D)^2$:

$$E(r) = E_0 \left[1 - \frac{1}{2}\left(exp\left(\frac{T(r)}{T_R}\right) - 1\right)\right] \qquad 9.$$

$$\nu(r) = \left(1 - \frac{E(r)}{E_0}\right)(\nu_{max} - \nu_{min}) + \nu_{min} \quad 10.$$

Temperature distribution is given by the infinite space conduction solution outside of $r = R$ (units degrees Celsius) $T(r) = (T_R - T_0)\frac{R}{r} + T_0$. Parameters are R = 1 km, D = 2 km, ν_{min} = 0.25, ν_{max} = 0.4, T_R = 1000 C, T_0 = 100 C, E_0 = 10 GPa, and P = 10 MPa.

In exercise 2C, exact solutions are not known so we use the average of all submitted FEM solutions as a reference solution to examine the variance in model results, after verifying that there are no visibly large outliers (Fig. 10, 11). Of the models used in these exercises, only FEMs can directly address material heterogeneity. Variance in all FEM solutions is less than 0.02 NRMSD, and some outlier FEM solutions are 3D so likely used coarser meshes for computational reasons.

We examine how well homogeneous models can approximate the heterogeneous models. A solution that uses the far field moduli values (ν = 0.25, E = 10 GPa) and the series expansion model of (Zhong et al., 2019) yields surface displacements that differ from the heterogeneous FEM solutions by 0.9 NRMSD, showing that the heterogeneity has a large impact in this scenario. We next determine what moduli values yield the best match (i.e., minimum NRMSD) to the heterogeneous solution "FEM 2D COMSOL J" by using a Nelder-Mead simplex inversion with bounds 0.25 < ν < 0.4, 0 < E < 10 GPa, and all other parameters fixed according to the exercise specifications. A solution with surface displacements that differ from the heterogeneous solution by only 0.1 NRMSD can be found with ν = 0.4 (the value right at the reservoir boundary) and E = 3.82 GPa (the value ~200 m from the reservoir boundary). This shows that in this scenario surface deformation is most sensitive to the elastic moduli very near the reservoir, and that a homogeneous model with elastic moduli representing those near the reservoir provides a reasonable approximation.

3. Inversion (validation) exercises

Source parameters inverted from surface deformation data can be non-unique due to variability in data processing, source model, and inversion methods. Ground based measurements include Global Navigation Satellite System (GNSS), tiltmeter, and strainmeter data. These have limited spatial coverage but high temporal resolution and accuracy (e.g., GNSS can provide mm accuracy for static positioning solutions and record 10s of samples per second). Remote sensing products include satellite Interferometric Synthetic Aperture Radar (InSAR), SAR amplitude correlation, airborne lidar, and structure-from-motion data. These typically only have temporal resolution of days but good spatial coverage (e.g., InSAR provides up to sub-cm accuracy and m-scale pixels depending on sensor platform). Each type of data has various sources of noise acting over different temporal and spatial scales. Inversions take a range of approaches for exploring model/parameter spaces depending on model parameter characteristics (linear vs. non-linear relations between model parameters and surface displacements) and inversion strategy (e.g., best-fit analyses vs. probabilistic approaches) and considering noise/uncertainty (Aster et al., 2018; Bagnardi and Hooper, 2018; Menke, 2018; Tarantola, 2004).

For this first phase of inversion exercises (exercise 3), we focus on static elastic displacements from spherical reservoirs. We provided synthetic ground displacement data in the form of an unrealistically dense 3-component GNSS survey with 400 (20x20) regularly spaced observation points; for comparison Kīlauea and Piton de la Fournaise are two of the best-monitored volcanoes and have ~75 and ~25 locations, respectively. We also provided ascending and descending line of sight (LOS) unwrapped InSAR interferograms (Fig. 12, Table 2).

Participants could use either or both types of data. Spatially uncorrelated noise was added to the modeled GNSS displacements, and spatially correlated noise (Fukushima et al., 2005) was added to the

InSAR data where correlation was a function of distance $C(r) = Vexp(r/\lambda)$ for variance V and correlation length λ. We provided two different datasets with different source parameters and noise levels; a low noise set with better signal/noise ratio than most real data and a high noise set (Table 3). However, we emphasize that these exercises will not directly indicate how effectively source parameters are estimated in real settings since we use simple source/earth/noise models, provide exact a-priori information about these factors, and provide displacements rather than having participants infer these from raw data (for which processing methods can differ). We note that all displacement data and InSAR LOS direction information was given to participants at limited precision (i.e., rounded), which introduces an additional source of error.

Participants were informed that the source model used to generate data was a series expansion solution for a pressurized spherical reservoir in a homogeneous elastic half space (Zhong et al., 2019), but other source models could be used in inversions (e.g., faster approximate solutions). We provided the elastic moduli (ν = 0.25, G = 10 GPa) and asked participants to estimate the source position (east, north, depth), radius, volume change, and pressure change.

3.1 Inversion exercise results

Exercise 3 results for the low and high noise datasets are shown in figures 13 and 14, and are grouped by the types of data and source models used. Solutions were submitted using Mogi and McTigue models, a dislocation BEM, a MBEM, a Gaussian process emulator, and the series expansion solution of (Zhong et al., 2019) (which was the true source model). Participants were not given instructions on what cost functions to use or on how to report their best estimates of parameters (e.g., minimum cost or maximum likelihood or maximum a posteriori) or confidence intervals, in order to exemplify the variability in these measures that are used in practice.

East and north locations are generally reported to be the best constrained parameters; estimates are roughly similar across all submissions but still have a range of ~300 m for both low and high noise datasets. We expect the overestimation of north coordinates in most submissions partly reflects a bias introduced by the added noise and/or data round-off error. Depth estimates have a range of ~400 m (or 20%) for low noise data and 800 m (or 35%) for high noise data. Volume change estimates have a range of 30% for low noise data and 50% for high noise data, pressure change estimates have a range of two orders of magnitude for both low and high noise data, and radius estimates have a range of one order of magnitude for both low and high noise data. With a Mogi model pressure change and radius cannot be separately resolved, while for many other source models pressure change and radius were directly inverted for and then volume changes were calculated given a formulation of reservoir elastic compressibility (often a full space approximation). However, for a spherical reservoir strong tradeoffs are generally expected between pressure change and source radius, particularly for higher depth/radius ratios (McTigue, 1987; Parks et al., 2012; Segall, 2010). One participant tested the effect of using MBEMs with three different upper bounds on radius, and found similar results for all parameters except pressure change. This highlights the need to use additional constraints in order to robustly constrain pressure changes and source radius in spherical reservoirs (Anderson et al., 2019).

Three participants conducted otherwise identical inversions for just InSAR data, just GNSS data, and both data types. There are appreciable differences in solutions depending upon the data type used, which emphasizes that care should be taken when comparing results for these exercises from solutions using different data types. Solutions generally show the lowest accuracy and highest reported uncertainty for just InSAR data; this occurs because even though the InSAR data contains more spatial points than the GNSS data the InSAR data only provides two displacement components and has spatially correlated noise.

Similar east and north location estimates were obtained with each type of source model, suggesting that

these parameters are not sensitive to source model choice. Depth, volume change, and pressure change show more sensitivity to source model choice, as expected (Dieterich and Decker, 1975), although the relative variation between different source models depends on the type of data and inversion methods used. For the same inversion method and type of data, the FEM emulator solution nearly exactly matches a Zhong solution for all parameters. The emulator solution also almost exactly matches the true low noise solution when both InSAR and GNSS data are used. We do not make one-to-one comparisons between other source models given that different inversion methods were used, but note that in most cases McTigue and Mogi solutions underestimate volume change, which suggests that when inversion methods are well calibrated source model choice can appreciably impact results even for sources with moderate depth/radius ratios such as in the low noise scenario (with ratio ~2.3). However, even a Mogi model can produce reasonable solutions for all data types and noise levels. In fact there is generally more variation between solutions using the same source model than between solutions using different source models, which suggests that much of the variance between estimates is dominated by inversion methods rather than by source model choice or even data types.

Importantly, for most parameters the variance between solutions exceeds the reported uncertainty of many of the solutions. We did not provide any instructions on how to estimate uncertainties in order to assess the methods used in practice. Most participants conducted probabilistic inversions, but with a variety of different parameter bounds/priors and sampling methods. Figure 15 shows PDFs (probability density functions) from a subset of the low noise estimates, as well as minimum reduced chi-square χ^2 misfits which provide complementary information about the parameter space. Reduced chi-square is calculated as $\chi^2 = (u^{obs} - u^{mod})^T C^{-1} (u^{obs} - u^{mod})$ for residual vector $(u^{obs} - u^{mod})$ and covariance matrix C, and provides a relatively direct way to visualize the cost function. PDFs represent an integral over the parameter space of likelihood L, which scales with the negative exponent of reduced chi-square $L \sim exp(-\chi^2)$, but can be multiplied by potentially non-uniform prior distributions and terms accounting for additional (potentially more difficult to quantify) sources of uncertainty (Aster et al., 2018). For this exercise such additional uncertainty would arise from using source models that only approximate the known source; in real applications uncertainty can arise from factors such as incomplete knowledge of data error properties (data uncertainty) and incomplete knowledge and/or accounting of complex earth structure (model uncertainty). For these exercises most participants followed the common practice of only considering data uncertainty.

The minimum reduced chi-square plots from a McTigue source (Fig. 15) show relatively pronounced global minima for east location, north location, and depth, but much broader minima for radius, volume change, and pressure change. Most submitted PDFs from MCMC (Markov Chain Monte Carlo) methods show comparatively narrow global maxima for all parameters, which is expected given the dense data we provided (which is typical for real InSAR data but not real GNSS networks), although some MCMC PDFs are much narrower than others. Many submitted PDFs from neighborhood algorithms used a smaller number of samples than the MCMC methods and show much broader PDFs, which could indicate that some of these PDFs are under-resolved. However, some of the neighborhood algorithm parameter estimates are still relatively accurate, and so in some cases (e.g., with computationally expensive forward models) there may be advantages to such methods that can use small sample numbers. Overall there is appreciable variability between different PDF submissions, even when accounting for the use of different types of data and source model. Some of these discrepancies might arise from using different downsampling methods, different (and potentially biased or overly-restrictive) prior distributions/parameter bounds, and/or from using different (or differently configured) methods for searching the parameter space (e.g., different numbers and distributions of samples).

4. Discussion

The importance of verifying models carefully prior to use is emphasized by the implementation errors that

our exercises revealed for several analytical forward models. Additionally, while most numerical forward models yielded roughly similar results, including multiple open-source FEM and BEM codes, some discrepancies highlight the importance of appropriate mesh refinement and boundary condition treatment. Care should also be taken when using constant dislocation BEMs, as their accuracy does not always increase with decreasing mesh size (Fig. 5) due to element edge singularity effects. The website for these exercises provides a starting point for model verification, but does not attempt to define accuracy thresholds as these may vary depending on application and user choices. For example, the models exhibited a wide range of reported computation times, and participants indicated that some models require considerably more time to learn to use and/or set up than others.

Both forward and inverse modeling exercises confirm that it is reasonable to use the approximate analytical Mogi or McTigue models for spherical reservoirs in homogeneous half spaces for moderate or high depth/radius ratios. For sources with lower depth/radius ratios, the inversion exercises suggest that more accurate source models can yield appreciably more accurate estimates of volume/pressure change and depth. In many scenarios, it will not be accurate to assume a spherical reservoir geometry and neglect topography or material heterogeneity. When the height/width ratio of topographic features is greater than or equal to ~0.3 (Segall, 2010) approximate topography corrections are generally not accurate, as is demonstrated with the Gaussian hill topography in exercise 2A. When the reservoir geometry is spheroidal, available analytical models will not always be reasonably accurate (depending upon source depth and radii), as is demonstrated for the shallow sill-like geometry in exercise 2B. Finally, exercise 2C shows that due to the strong temperature dependence of E and ν (Bakker et al., 2016), neglecting radial heterogeneity in elastic moduli around a spherical reservoir with a steady-state conduction temperature profile can appreciably impact predicted deformation. In this scenario a model using homogeneous elastic moduli with near-reservoir values can provide a reasonable approximation (Fig. 10,11), suggesting that geodetic inversions assuming homogeneity (Anderson and Poland, 2016) will find moduli corresponding most closely to high-temperature values near the reservoir. However, these exercises do not consider other sources of host rock heterogeneity such as vertical layering (Masterlark, 2007) or viscoelastic effects (Dragoni and Magnanensi, 1989). Approaches that seek realistic spatial variability in material properties with constraints from geophysical images are promising (Hickey et al., 2016), although more studies are needed to address how well heterogeneity can be resolved and/or approximated in various conditions.

All of the numerical methods required computation times of seconds or longer, which is orders of magnitude longer than most analytical solutions. Reported computation times for FEMs ranged widely from seconds to tens of minutes, even when considering only 2D solutions, although some of this variation is likely due to differences in the discretization and computational resources used. BEMs are more computationally efficient than FEMs, which will be particularly advantageous when 3D models are required, but are mostly limited to homogeneous problems. It is feasible to conduct probabilistic inversions with forward model computation times of seconds, although doing so will require more computational resources and/or fewer samples than could be used with faster forward models, and thus will potentially result in less accurate PDFs. Fictitious domain approaches are being developed that could enable numerical models to be used more efficiently in inversions (Bodart et al., 2022, 2016). These exercises demonstrated that an emulator can provide high accuracy at low computational cost for spheroidal reservoirs in a homogeneous half space. However, further work is needed to develop emulators that consider more complex source geometries, topography, and heterogeneous rheology; this could require larger training times and/or building emulators specific to particular volcanoes over particular time periods (Anderson and Gu, 2023).

Even in the unrealistically ideal scenario of having dense low-noise datasets and a known source model, appreciably different estimates for many parameters were obtained in the inversion exercises.

Additionally, many reported confidence bounds do not overlap with other estimates or with the true solutions. For spherical sources, some tradeoffs between pressure change, radius, volume change, and depth are expected (Parks et al., 2012). However, there were also appreciable differences in east and north locations. Differences in inversion methods appear to be a primary driver of this variability, which emphasizes that even for simple source models it is vital to carefully test inversions against synthetic data and ensure comprehensive exploration of parameter spaces. These exercises provide some standardized tests that can be a starting point, although additional problem-specific testing will also generally be needed since parameter space exploration can be more difficult for more complex source models and sparser/noisier data. Finally, the appreciable discrepancies between many reported confidence bounds emphasizes the importance of comprehensively calculating and reporting uncertainty. This could include clearly specifying what sources of uncertainty (e.g., model error, data variance) are considered, using hyperparameters to account for model uncertainty, and displaying PDFs and/or cost functions.

5. Future directions

These exercises only considered static elastic displacements from spheroidal reservoirs, and only tested inversions for spherical sources from already processed data. Since several implementation errors and discrepancies between solutions were found even for these simple scenarios, this project has demonstrated the vital importance of community verification and validation exercises. Anecdotes also indicate that these exercises have been a useful learning tool. Using the SCEC earthquake verification and validation exercises as template, we anticipate benefits in expanding these exercises to more complex problems in volcano deformation. Important forward modeling scenarios include time-dependent poro-visco-elastic-plastic host rock response, sheet intrusions, multiple deformation sources, hydrothermal fluid circulation, and surface loading. Important inversion scenarios include providing raw time-series data to test all stages of data processing workflows, testing dikes and complex/multicomponent sources, and systematically studying different inversion approaches and uncertainty quantification to handle model complexity without overfitting. Like the SCEC exercises, this will likely require multiple concurrent efforts. We see great potential for community building by developing exercises around data for real volcanoes, ideally with additional constraints on the magmatic system from other sources beyond deformation.

Finally, we expect that model verification and validation exercises could be expanded to several other aspects of volcano science with great effect. Model intercomparison has been conducted for conduit flow (Sahagian, 2005), lava flows (Dietterich et al., 2017), plumes (Costa et al., 2016), and pyroclastic density currents (Esposti Ongaro et al., 2020). These efforts should be extended in common, rigorous, and sustained frameworks to advance volcano science, monitoring, and hazard forecasting.

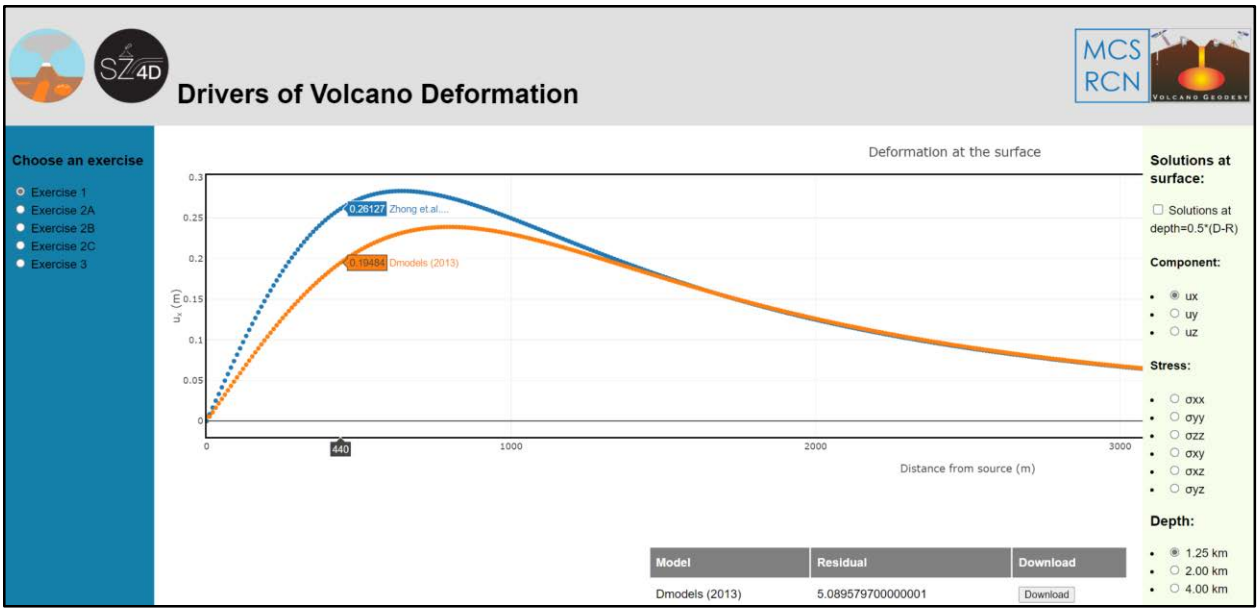

Figure 1. Screenshot showing interactive plotting on the project website (http://www.driversofvolcanodeformation.org).

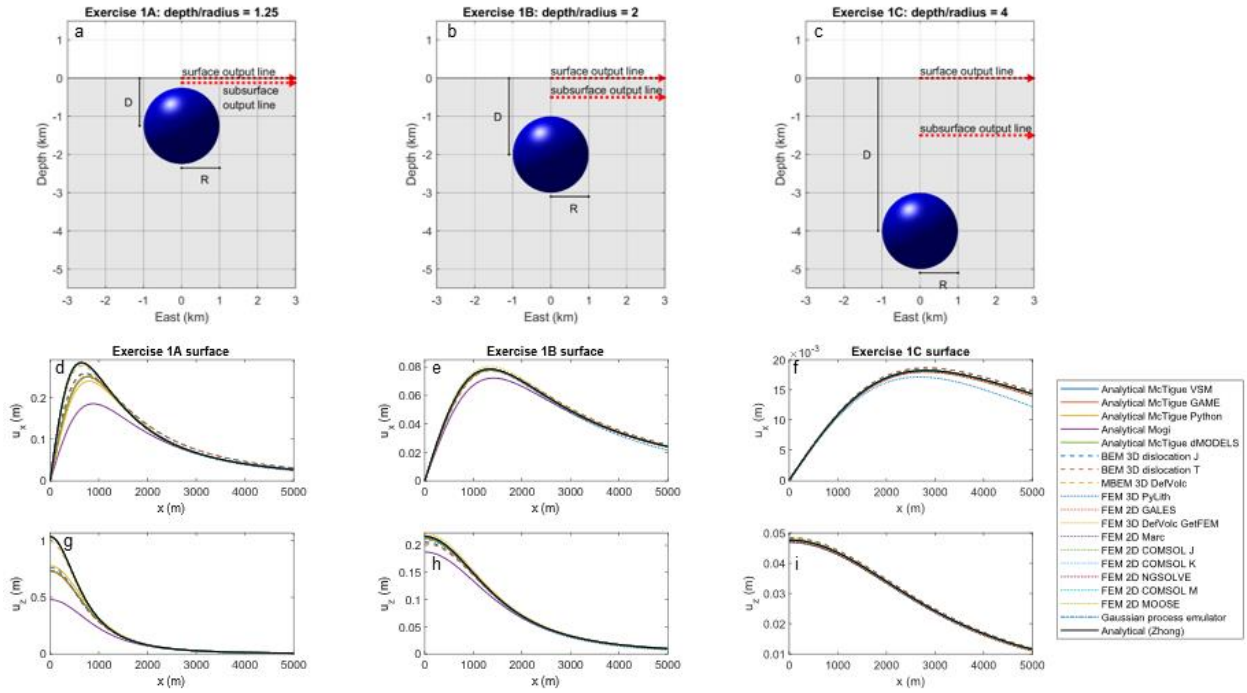

Figure 2. Exercise 1: sphere in a homogeneous half space. (a-c) Problem geometry, with dashed output lines indicating the transects along which solutions are reported at 10 m intervals out to a distance of 5 km. (d-i) Surface displacement submissions.

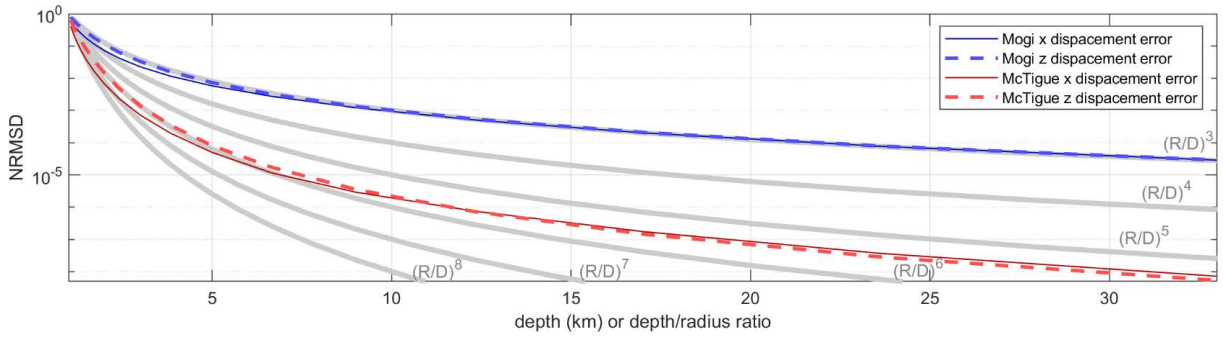

Figure 3. Convergence of surface displacements from approximate analytical Mogi and McTigue models relative to the series expansion solution of (Zhong et al., 2019) for different radius/depth (R/D) ratios. Several different order polynomials are shown for comparison. Error at a single location (rather than the aggregate NRMSD metric) would generally more closely follow the theoretical accuracy of $(R/D)^3$ for the Mogi model and $(R/D)^6$ for the McTigue model.

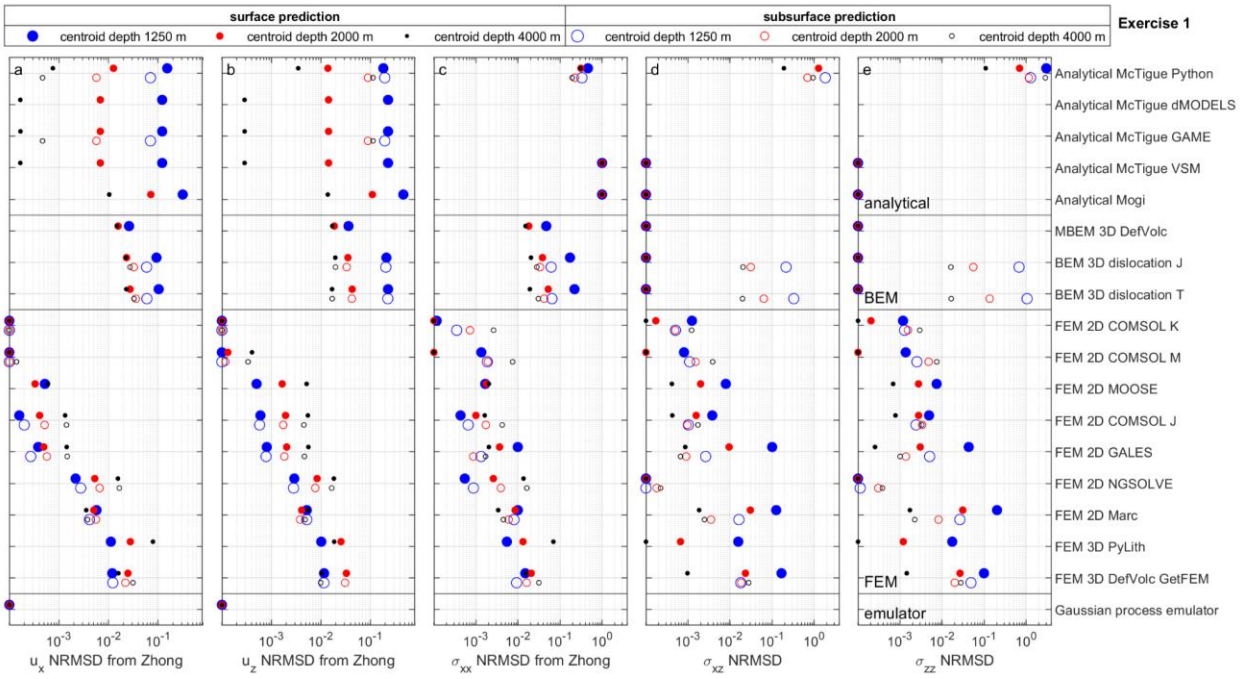

Figure 4. Normalized root mean squared difference (NRMSD) for all exercise 1 (sphere in a homogeneous half space) submissions compared to the series expansion solution of (Zhong et al., 2019). Values less than the x-axis bounds are plotted at the bounds. The modified NRMSD metric normalized by source pressure is used for σ_{zz} and σ_{xz} at the free surface (d-e).

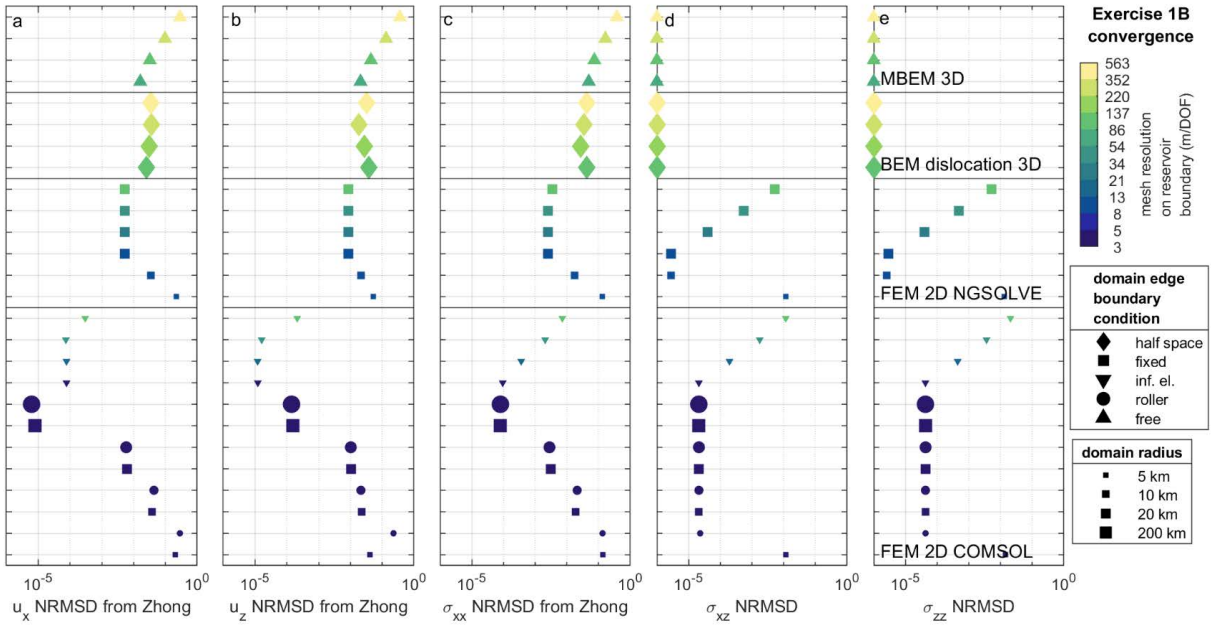

Figure. 5. Convergence of the normalized root mean square difference (NRMSD) of selected numerical methods compared to the series expansion solution of (Zhong et al., 2019) for different mesh/boundary treatments in exercise 1B (sphere in a homogeneous half space, centroid depth 2 km). Values less than 10^{-6} are plotted at 10^{-6}. The modified NRMSD metric normalized by source pressure is used for σ_{zz} and σ_{xz} at the free surface (d-e). Mesh resolution is shown by the average distance per degree of freedom (m/DOF) along the reservoir boundary; this is equal to average element size divided by element order (1 for both BEMs, 4 for NGSOLVE, and 2 for COMSOL®). Marker sizes indicate domain radius and shapes indicate outer boundary conditions (BC): diamonds for half space BEMs with no outer boundary, squares for “fixed” BC (zero displacement), circles for “roller” BC (zero normal displacement plus zero tangential traction), and triangles for “infinite element” BC (using coordinate transformations to approximate an infinite domain).

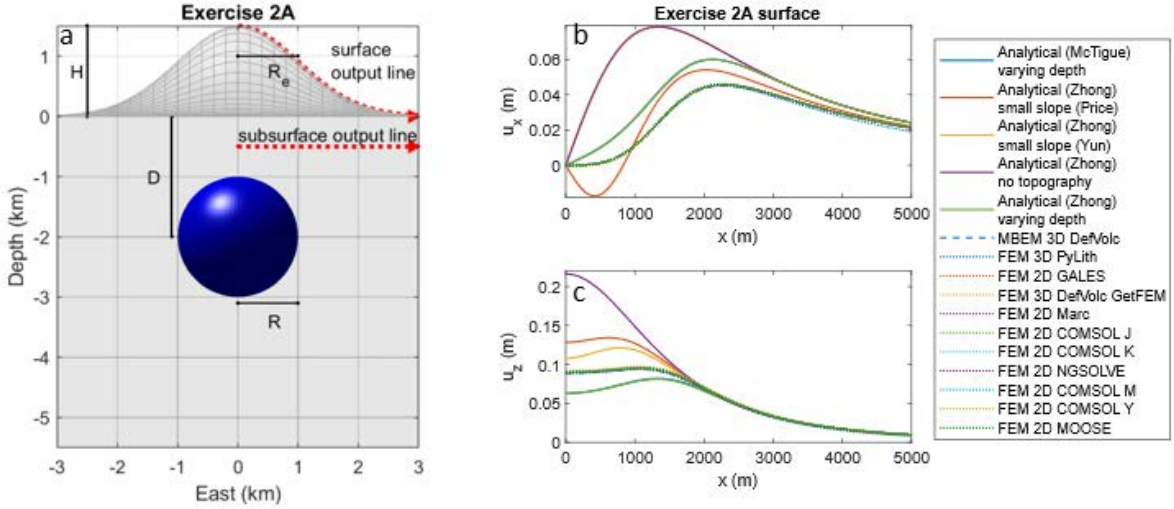

Figure 6. Exercise 2A: sphere in a homogeneous half space with Gaussian topography. (a) Problem

geometry, with dashed output lines indicating the transects along which solutions are reported at 10 m intervals out to a distance of 5 km. (b-c) Surface displacement submissions.

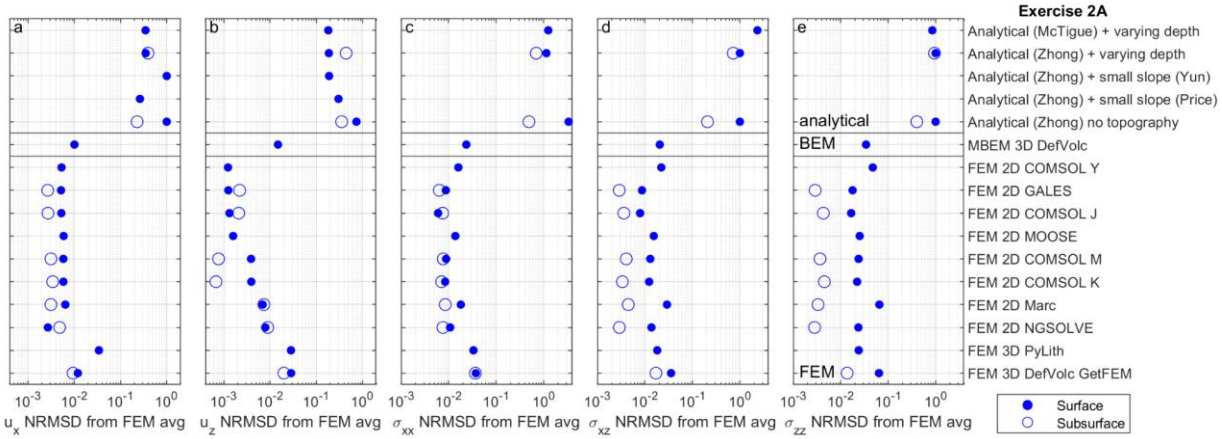

Figure 7. Normalized root mean squared difference (NRMSD) for all exercise 2A (sphere in a homogeneous half space with Gaussian topography) submissions relative to the average FEM solution. In this case the NRMSD metric indicates variability between solutions rather than error or accuracy, and the FEM average may be biased (e.g., due to overrepresenting COMSOL®). For this exercise the NRMSD expression in equation 3 is used for all solution components since the topography makes σ_{zz} and σ_{xz} non-zero at the free surface. The label "varying depth" indicates the zeroth-order topographic correction of (Williams and Wadge, 1998), and "small slope" indicates the first-order topographic correction of (Williams and Wadge, 2000) (for which two different implementations were tested).

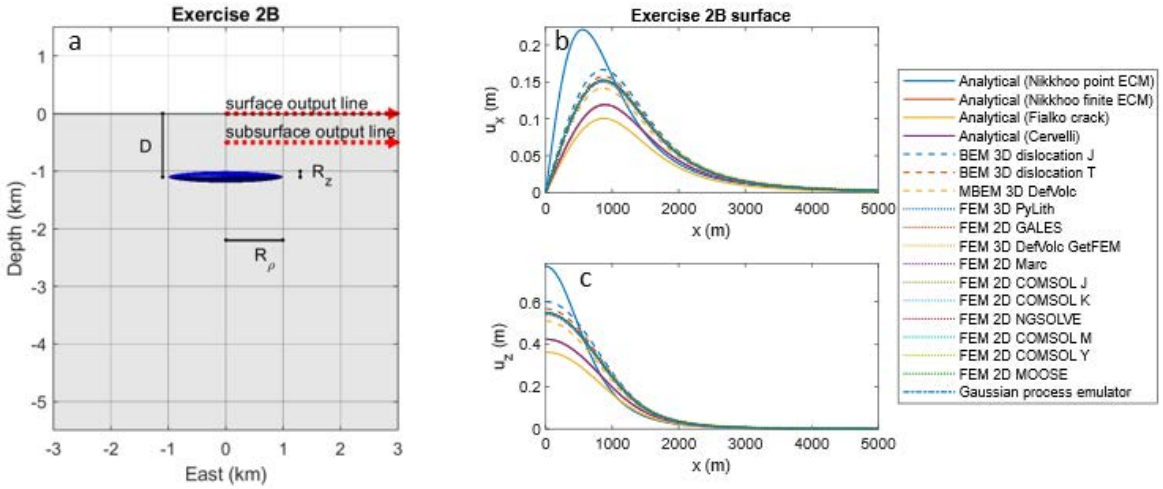

Figure 8. Exercise 2B: oblate spheroid in a homogeneous half space. (a) Problem geometry, with dashed output lines indicating the transects along which solutions are reported at 10 m intervals out to a distance of 5 km. (b-c) Surface displacement submissions.

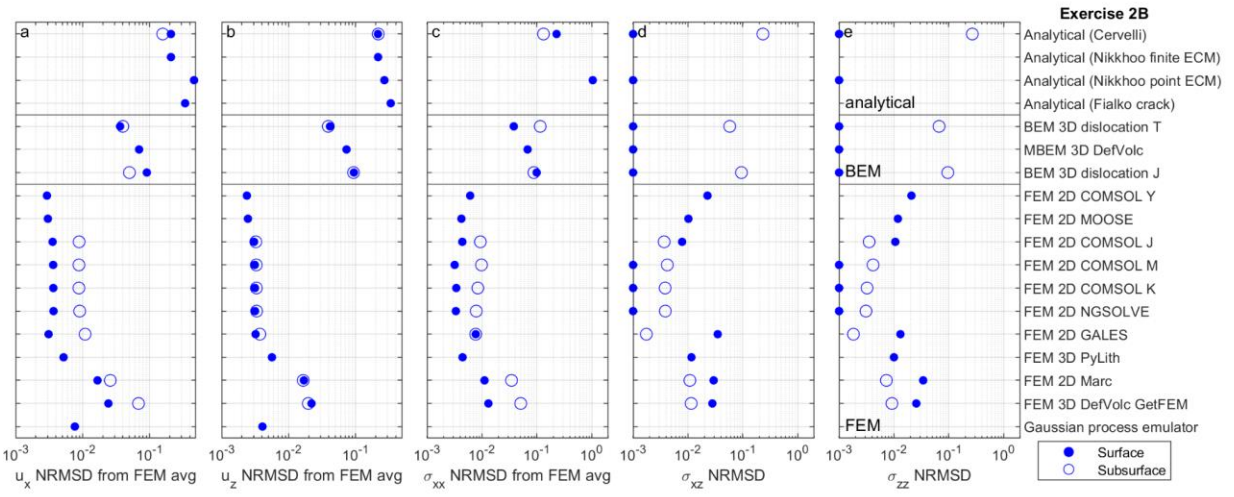

Figure 9. Normalized root mean squared difference (NRMSD) for all exercise 2B (oblate spheroid in a homogeneous half space) submissions relative to the average FEM solution. In this exercise the NRMSD metric indicates variability between solutions rather than error or accuracy, except for σ_{zz} and σ_{xz} at the free surface where the modified NRMSD metric normalized by source pressure is used (d-e). The FEM average may be biased (e.g., due to overrepresenting COMSOL®). Values less than the x-axis bounds are plotted at the bounds.

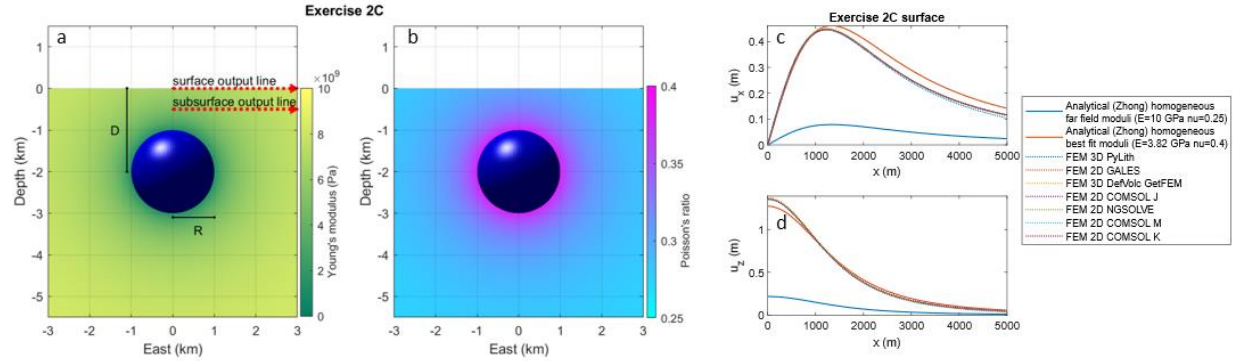

Figure 10. Exercise 2C: sphere in a heterogeneous half space. (a-b) Problem geometry and elastic moduli, with dashed output lines indicating the transects along which solutions are reported at 10 m intervals out to a distance of 5 km. (c-d) Surface displacement submissions.

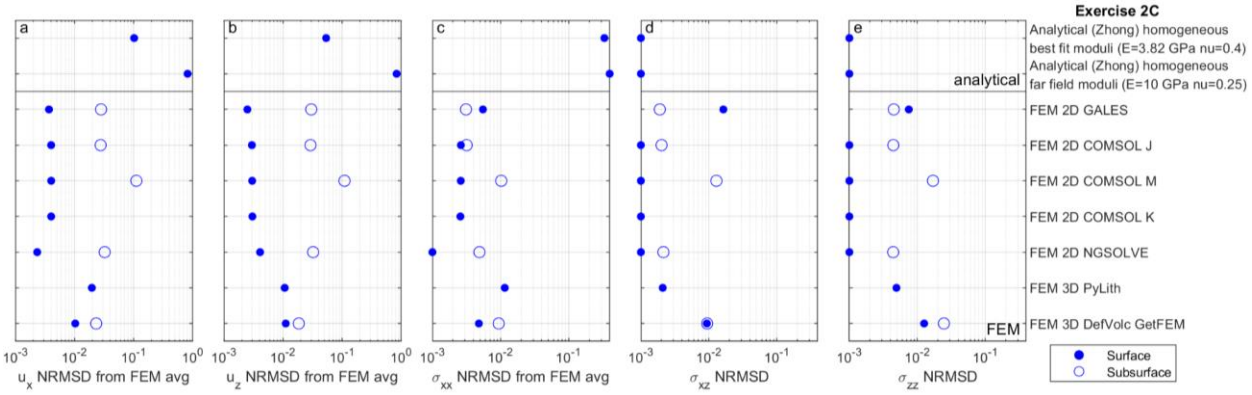

Figure 11. Normalized root mean squared difference (NRMSD) for all exercise 2C (sphere in a heterogeneous half space) submissions relative to the average FEM solution. In this exercise the NRMSD metric indicates variability between solutions rather than error or accuracy, except for σ_{zz} and σ_{xz} at the free surface where the modified NRMSD metric normalized by source pressure is used (d-e). The FEM average may be biased (e.g., due to overrepresenting COMSOL®). Values less than the x-axis bounds are plotted at the bounds.

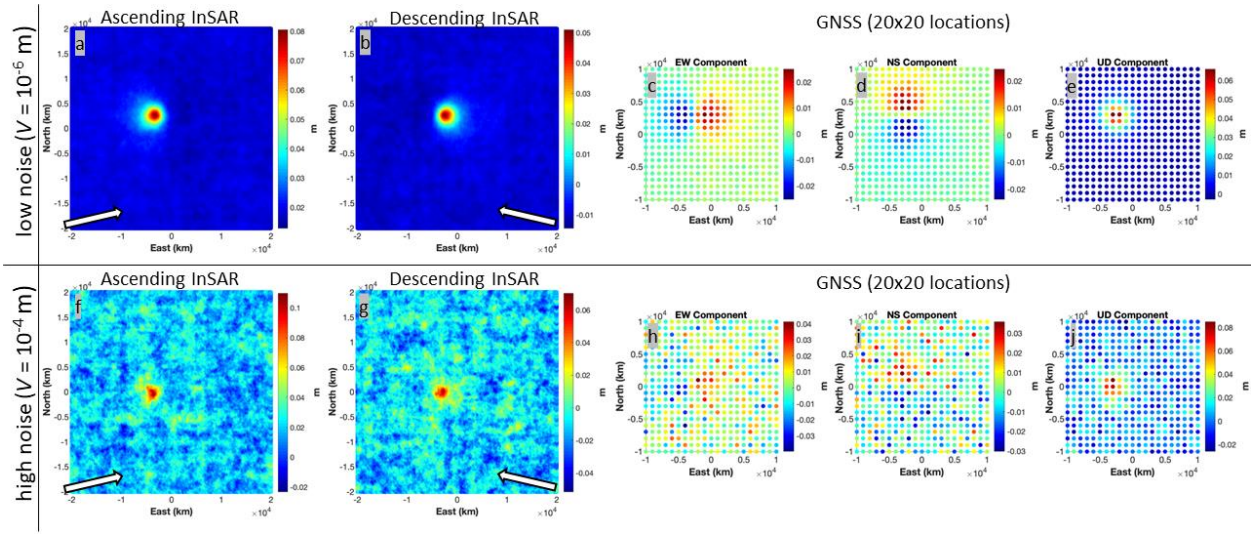

Figure 12. Synthetic data for exercise 3 inversions. (a-b) Low noise InSAR data. (c-e) Low noise GNSS data. (f-g) High noise InSAR data. (h-j) High noise GNSS data.

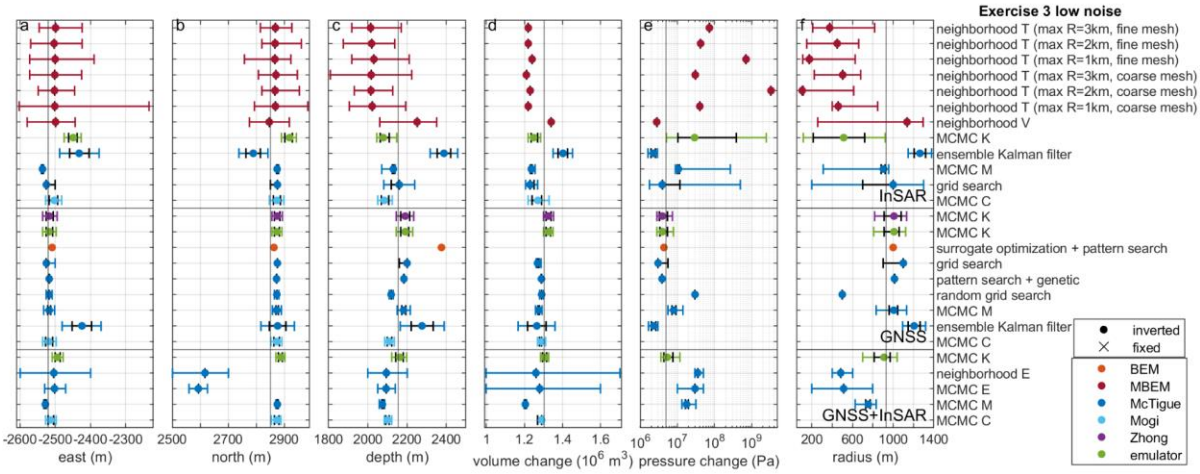

Figure 13. Exercise 3 low noise parameter estimates. Vertical black lines are true solutions that correspond to a depth/radius ratio of ~2.3. Black and colored bars indicate 64% and 95% confidence bounds, respectively. Some participants did not report bounds or only reported one set of bounds. For source models except the Mogi source and Gaussian process emulator, volume change (d) is not inverted directly. Estimates of InSAR offsets are not shown.

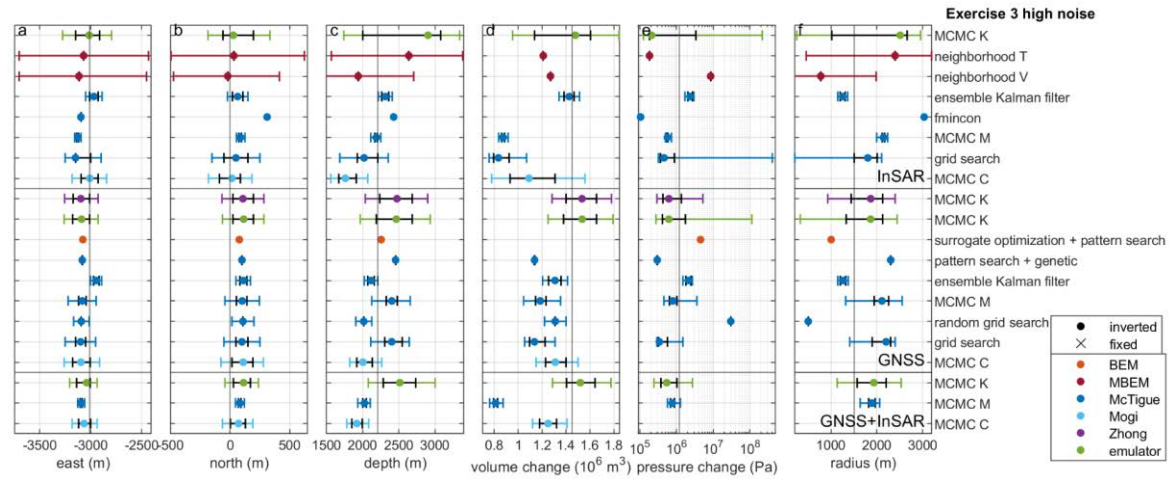

Figure 14. Exercise 3 high noise parameter estimates. Vertical black lines are true solutions that correspond to a depth/radius ratio of ~1.5. Black and colored bars indicate 64% and 95% confidence bounds, respectively. Some participants did not report bounds or only reported one set of bounds. For source models except the Mogi source and Gaussian process emulator, volume change (d) is not inverted directly. Estimates of InSAR offsets are not shown.

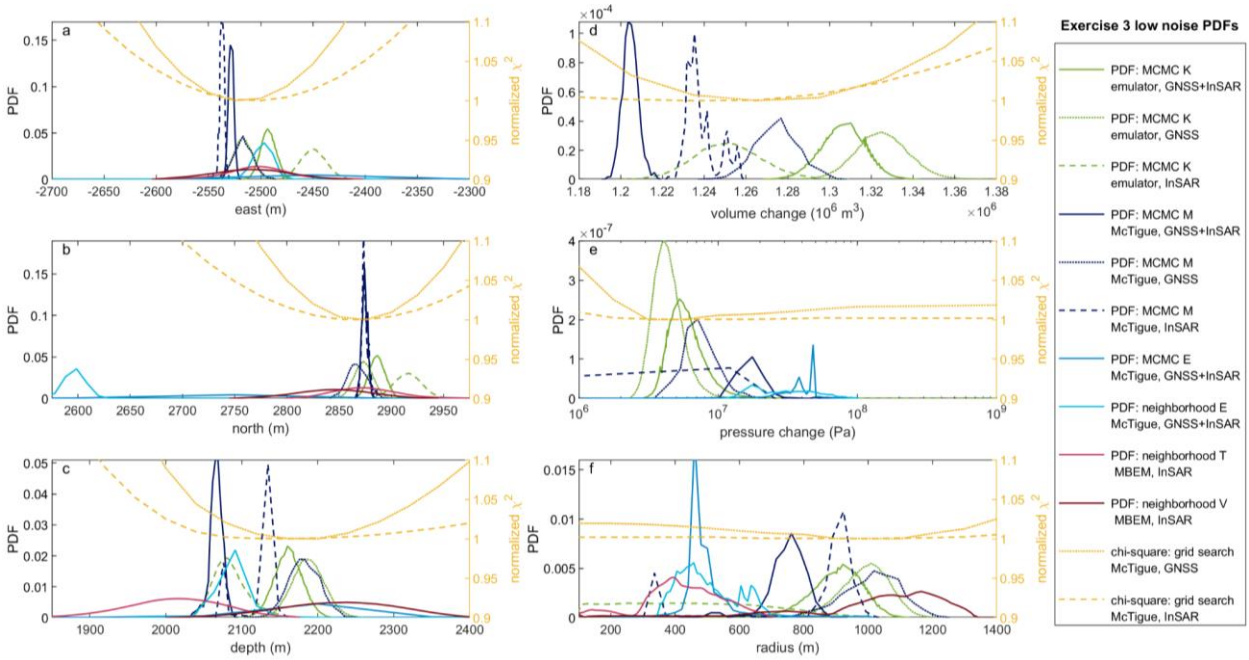

Figure 15. Probability density functions (PDFs) from a subset of the exercise 3 low noise submissions. For source models except the Gaussian process emulator, volume change (d) is not inverted directly. Coarser parameter resolution provided with some submissions causes angular PDF appearances. Yellow lines (right axes) show the minimum reduced chi-square χ^2 misfit (normalized so that the minimum is 1) that can be obtained with a McTigue model based on grid searches over the parameter space.

description	submitter	element size on reservoir (m)	domain radius (km)	domain edge boundary condition	compute time order of magnitude (s)	reference
Analytic Zhong	Crozier	none (64th order expansion)			100	corrected from (Zhong et al., 2019)
Analytic McTigue dMODELS	Kim	none				(Battaglia et al., 2013)
Analytic McTigue python	Angarita	none				
Analytic Mctigue GAME	Cannavo	none				(Cannavò, 2019)
Analytic McTigue VSM	Astort	none				(Trasatti, 2022)
Analytic Mogi	Crozier	none			0.01	implemented based on (Mogi, 1958)
Analytic Cervelli	Crozier	none			0.01	(Cervelli, 2013)
Analytic Nikkhoo point ECM	Crozier	none			0.01	(Nikkhoo et al., 2017)
Analytic Nikkhoo finite ECM	Crozier	none (10000 points)			0.1	(Nikkhoo and Rivalta, 2022)
Analytic Fialko Crack	Crozier	none (2 integration intervals, tolerance 1E-6)			0.1	(Fialko et al., 2001)

MBEM 3D DEFVOLC	Shreve	70	20	free	100	(Cayol and Cornet, 1997)
BEM 3D dislocation J	Crozier	140	none		100	use triangular dislocations from (Nikkhoo and Walter, 2015)
BEM 3D dislocation T	Wang	35	none		1000	use triangular dislocations from (Nikkhoo and Walter, 2015)
FEM 2D COMSOL K	Anderson	1	120	inf. el.	10	COMSOL Multiphysics®
FEM 2D COMSOL M	Head	10	20	inf. el	1	COMSOL Multiphysics®
FEM 2D MOOSE	Zhan			roller	1	(Lindsay et al., 2022)
FEM 2D COMSOL J	Crozier	100	50	fixed	10	COMSOL Multiphysics®
FEM 2D GALES	Garg	10	50	fixed	1	(Garg et al., 2021; Longo et al., 2012)
FEM 2D NGSOLVE	Karlstrom & Rucker	50	20	fixed	10	(Rucker et al., 2022)
FEM 2D Marc	Silverii	50	80	roller		MSC Software Marc®
FEM 3D PyLith	Iozzia & Currenti	50	10	fixed	10000	(Aagaard et al., 2013)
FEM 3D DefVolc GetFEM	Dabaghi		20	fixed	1000	DefVolc fictitious domain based on getFEM++ (Bodart et al., 2022, 2020)
Gaussian process emulator	Anderson	trained on FEMs similar to "FEM 2D COMSOL K" above			0.001	(Anderson and Gu, 2023; Anderson et al., 2019)

Table 1. Forward model submission information. "2D" indicates 2D axi-symmetric models. For outer domain edge boundary conditions "fixed" is zero displacement, "roller" is zero normal displacement plus zero tangential traction, "inf. el." (infinite element) uses coordinate transformations to approximate an infinite domain, and "free" is zero traction. Mesh and domain size values are approximate representative values; some participants used different discretization orders, used meshes with variable element sizes along the reservoir, and/or used slightly different mesh and domain sizes for different exercises. Only order of magnitude computation times are shown as participants reported computation times on different hardware.

	Azimuth	Incidence	LOS x	LOS y	LOS z	Offset (m)
ascending	-11.514	33.901	-0.54	-0.11	0.83	0.018
descending	-165.960	36.870	0.56	-0.14	0.80	-0.010

Table 2. Synthetic InSAR properties for both high noise and low noise datasets. The directions to satellites are given in terms of azimuth and incidence angles (from vertical) or line of sight (LOS) unit vectors.

	GNSS + InSAR variance V (m)	InSAR correlation length λ (m)	east position (m)	north position (m)	depth D (m)	radius R (m)	pressure P (Pa)	Volume change (m^3)

low noise	1E-6	750	-2520	2850	2155	930	5.0E6	1.30E6
high noise	1E-4	750	-3010	0	2205	1500	1.19E6	1.45E6

Table 3. Synthetic data source parameters for inversion exercises (exercise 3). Only the first two columns (noise parameters) were given to participants during the exercises.

description	submitter	source model	downsampling (InSAR)	inverse method
neighbor-hood T	Shreve	MBEM, 1280 reservoir elements and 20 km domain radius with 23940 ground surface elements (Cayol and Cornet, 1997)	Quadtree (Jonsson, 2002), 1836 points	Neighborhood algorithm (Fukushima et al., 2005), 34 iterations, 2016 forward models, appraisal on 10000 points
neighbor-hood V	Cayol	MBEM, 1280 reservoir elements and 20 km domain radius with 3470 ground surface elements (Cayol and Cornet, 1997)	Quadtree (Jonsson, 2002), 986 points	Neighborhood algorithm (Fukushima et al., 2005), 38 iterations, 1924 forward models, appraisal on 10000 points
MCMC K (Zhong)	Anderson	Zhong series expansion (Zhong et al., 2019)	Quadtree (Jonsson, 2002), 1420 points	Bayesian MCMC, uniform priors, 600000 samples
MCMC K (emulator)	Anderson	Gaussian process FEM emulator (Anderson and Gu, 2023; Anderson et al., 2019)	Quadtree (Jonsson, 2002), 1420 points	Bayesian MCMC, uniform priors, 600000 samples
ensemble Kalman filter	Zhan	McTigue python		30 iterations
MCMC M	Angarita	McTigue python VMOD	Quadtree, controlled by variance in non-local means filter, 1942 points	Bayesian MCMC with 1000000 samples
grid search	Crozier	McTigue dMODELS (Battaglia et al., 2013)	Uniform, gaussian filter, 1681 points	Coarser resolution then finer resolution grid search, uniform priors, reduced chi square, 2000000 samples
MCMC C	Novoa	Mogi GBIS (Bagnardi and Hooper, 2018)	Circular quadtree, 2944 points	Bayesian MCMC (Bagnardi and Hooper, 2018)
surrogate optimization + pattern search	Wang	Mogi then dislocation BEM using 5012 triangular elements (Nikkhoo and Walter, 2015) with radius fixed to 1 km		MATLAB® surrogate optimization with Mogi for 1000 iterations, then MATLAB® pattern search with BEM for 10 iterations, unweighted L2 norm
pattern search + genetic	Cannavò	McTigue GAME (Cannavò, 2019)		Pattern search with genetic algorithms
random grid search	Le Mével	McTigue dMODELS (Battaglia et al., 2013)		Random grid search, weighted least squares
MCMC E	Trasatti	McTigue VSM (Trasatti, 2022)	Personal subsampling algorithm, uniform in different areas	Bayesian MCMC (Trasatti, 2022)

neighbor-hood E	Trasatti	McTigue VSM (Trasatti, 2022)	Personal subsampling algorithm, uniform in different areas	Neighborhood algorithm global optimization
fmincon	Kim	McTigue dMODELS (Battaglia et al., 2013)		MATLAB® fmincon, chi square

Table 4. Inversion submission information.

Bibliography

Aagaard, B.T., Knepley, M.G., Williams, C.A., 2013. A domain decomposition approach to implementing fault slip in finite-element models of quasi-static and dynamic crustal deformation. J. Geophys. Res. Solid Earth 118, 3059–3079. https://doi.org/10.1002/jgrb.50217.

Amoruso, A., Crescentini, L., 2013. Analytical models of volcanic ellipsoidal expansion sources. Annals of Geophysics 56. https://doi.org/10.4401/ag-6441.

Amoruso, A., Crescentini, L., 2011. Modelling deformation due to a pressurized ellipsoidal cavity, with reference to the Campi Flegrei caldera, Italy. Geophys. Res. Lett. 38. https://doi.org/10.1029/2010GL046030.

Anderson, K.R., Gu, M., 2023. Emulation of volcano deformation sources using machine learning models: a Gaussian process-based approach.

Anderson, K.R., Johanson, I.A., Patrick, M.R., Gu, M., Segall, P., Poland, M.P., Montgomery-Brown, E.K., Miklius, A., 2019. Magma reservoir failure and the onset of caldera collapse at Kīlauea Volcano in 2018. Science 366. https://doi.org/10.1126/science.aaz1822.

Anderson, K.R., Poland, M.P., 2016. Bayesian estimation of magma supply, storage, and eruption rates using a multiphysical volcano model: Kīlauea Volcano, 2000–2012. Earth and Planetary Science Letters 447, 161–171. https://doi.org/10.1016/j.epsl.2016.04.029.

Aster, R.C., Borchers, B., Thurber, C.H., 2018. Parameter estimation and inverse problems. Elsevier.

Bagnardi, M., Hooper, A., 2018. Inversion of surface deformation data for rapid estimates of source parameters and uncertainties: A bayesian approach. Geochem. Geophys. Geosyst. 19, 2194–2211. https://doi.org/10.1029/2018GC007585.

Bakker, R.R., Frehner, M., Lupi, M., 2016. How temperature-dependent elasticity alters host rock/magmatic reservoir models: A case study on the effects of ice-cap unloading on shallow volcanic systems. Earth and Planetary Science Letters 456, 16–25. https://doi.org/10.1016/j.epsl.2016.09.039.

Barall, M., Harris, R.A., 2015. Metrics for comparing dynamic earthquake rupture simulations. Seismological Research Letters 86, 223–235. https://doi.org/10.1785/0220140122.

Bato, M.G., Lundgren, P., Pinel, V., Solidum, R., Daag, A., Cahulogan, M., 2021. The 2020 eruption and large lateral dike emplacement at taal volcano, philippines: insights from satellite radar data. Geophys. Res. Lett. 48. https://doi.org/10.1029/2021GL092803.

Battaglia, M., Cervelli, P.F., Murray, J.R., 2013. dMODELS: A MATLAB software package for modeling crustal deformation near active faults and volcanic centers. Journal of Volcanology and Geothermal Research 254, 1–4. https://doi.org/10.1016/j.jvolgeores.2012.12.018.

Bodart, O., Cayol, V., Court, S., Koko, J., 2016. XFEM-Based Fictitious Domain Method for Linear Elasticity Model with Crack. SIAM J. Sci. Comput. 38, B219–B246. https://doi.org/10.1137/15M1008385.

Bodart, O., Cayol, V., Dabaghi, F., Koko, J., 2022. An inverse problem in an elastic domain with a crack : a fictitious domain approach. Comput. Geosci. 26, 423–435. https://doi.org/10.1007/s10596-021-10121-7.

Bodart, O., Cayol, V., Dabaghi, F., Koko, J., 2020. Fictitious domain method for an inverse problem in volcanoes, in: Haynes, R., MacLachlan, S., Cai, X.-C., Halpern, L., Kim, H.H., Klawonn, A., Widlund,

O. (Eds.), Domain Decomposition Methods in Science and Engineering XXV, Lecture Notes in Computational Science and Engineering. Springer International Publishing, Cham, pp. 409–416. https://doi.org/10.1007/978-3-030-56750-7_47.

Cannavò, F., 2019. A new user-friendly tool for rapid modelling of ground deformation. Comput. Geosci. 128, 60–69. https://doi.org/10.1016/j.cageo.2019.04.002.

Cayol, V., Cornet, F.H., 1997. 3D mixed boundary elements for elastostatic deformation field analysis. International Journal of Rock Mechanics and Mining Sciences 34, 275–287. https://doi.org/10.1016/S0148-9062(96)00035-6.

Cayol, V., Karlstrom, L., Montgomery-Brown, E., Bato, M.G., Angarita-Vargas, M., Grapenthin, R., Anderson, K., Astort, A., Bodart, O., Cannavo, F., Currenti, G., Dabaghi, F., Garg, D., Head, M., Iozzia, A., Le Mevel, H., McCluskey, O., Novoa, C., Silverii, F., Trasatti, E., Zhan, Y., 2023. Drivers of Volcano Deformation (DVD) validation and verification exercises: Phase 1. Presented at the IUGG, IUGG.

Cervelli, P., 2013. Analytical Expressions for Deformation from an Arbitrarily Oriented Spheroid in a Half-Space. http://volcanoes.usgs.gov/software/spheroid.

Coco, A., Currenti, G., Negro, C.D., Russo, G., 2014. A Second Order Finite-Difference Ghost-Point Method for Elasticity Problems on Unbounded Domains with Applications to Volcanology. Commun. Comput. Phys. 16, 983–1009. https://doi.org/10.4208/cicp.210713.010414a.

Costa, A., Suzuki, Y.J., Cerminara, M., Devenish, B.J., Ongaro, T.E., Herzog, M., Van Eaton, A.R., Denby, L.C., Bursik, M., de' Michieli Vitturi, M., Engwell, S., Neri, A., Barsotti, S., Folch, A., Macedonio, G., Girault, F., Carazzo, G., Tait, S., Kaminski, E., Mastin, L.G., Bonadonna, C., 2016. Results of the eruptive column model inter-comparison study. Journal of Volcanology and Geothermal Research 326, 2–25. https://doi.org/10.1016/j.jvolgeores.2016.01.017.

Crouch, S.L., Starfield, A.M., 1983. Boundary element methods in solid mechanics: With applications in rock mechanics and geological engineering. London.

Dieterich, J.H., Decker, R.W., 1975. Finite element modeling of surface deformation associated with volcanism. J. Geophys. Res. 80, 4094–4102. https://doi.org/10.1029/JB080i029p04094.

Dietterich, H.R., Lev, E., Chen, J., Richardson, J.A., Cashman, K.V., 2017. Benchmarking computational fluid dynamics models of lava flow simulation for hazard assessment, forecasting, and risk management. J. Appl. Volcan. 6, 9. https://doi.org/10.1186/s13617-017-0061-x.

Dragoni, M., Magnanensi, C., 1989. Displacement and stress produced by a pressurized, spherical magma chamber, surrounded by a viscoelastic shell. Physics of the Earth and Planetary Interiors 56, 316–328. https://doi.org/10.1016/0031-9201(89)90166-0.

Dumont, Q., Cayol, V., Froger, J.-L., Peltier, A., 2022. 22 years of satellite imagery reveal a major destabilization structure at Piton de la Fournaise. Nat. Commun. 13, 2649. https://doi.org/10.1038/s41467-022-30109-w.

Ebmeier, S.K., Andrews, B.J., Araya, M.C., Arnold, D.W.D., Biggs, J., Cooper, C., Cottrell, E., Furtney, M., Hickey, J., Jay, J., Lloyd, R., Parker, A.L., Pritchard, M.E., Robertson, E., Venzke, E., Williamson, J.L., 2018. Synthesis of global satellite observations of magmatic and volcanic deformation: implications for volcano monitoring & the lateral extent of magmatic domains. J. Appl. Volcan. 7, 2. https://doi.org/10.1186/s13617-018-0071-3.

Erickson, B.A., Jiang, J., Barall, M., Lapusta, N., Dunham, E.M., Harris, R., Abrahams, L.S., Allison, K.L., Ampuero, J.-P., Barbot, S., Cattania, C., Elbanna, A., Fialko, Y., Idini, B., Kozdon, J.E., Lambert, V., Liu, Y., Luo, Y., Ma, X., Best McKay, M., Wei, M., 2020. The community code verification exercise for simulating sequences of earthquakes and aseismic slip (SEAS). Seismological Research Letters 91, 874–890. https://doi.org/10.1785/0220190248.

Esposti Ongaro, T., Cerminara, M., Charbonnier, S.J., Lube, G., Valentine, G.A., 2020. A framework for validation and benchmarking of pyroclastic current models. Bull. Volcanol. 82, 51. https://doi.org/10.1007/s00445-020-01388-2.

Fernández, J., Pepe, A., Poland, M.P., Sigmundsson, F., 2017. Volcano Geodesy: Recent developments and future challenges. Journal of Volcanology and Geothermal Research 344, 1–12. https://doi.org/10.1016/j.jvolgeores.2017.08.006.

Fialko, Y., Khazan, Y., Simons, M., 2001. Deformation due to a pressurized horizontal circular crack in an elastic half-space, with applications to volcano geodesy. Geophys. J. Int. 146, 181–190. https://doi.org/10.1046/j.1365-246X.2001.00452.x.

Fournier, N., Chardot, L., 2012. Understanding volcano hydrothermal unrest from geodetic observations: Insights from numerical modeling and application to White Island volcano, New Zealand. J. Geophys. Res. 117. https://doi.org/10.1029/2012JB009469.

Fukushima, Y., Cayol, V., Durand, P., 2005. Finding realistic dike models from interferometric synthetic aperture radar data: The February 2000 eruption at Piton de la Fournaise. J. Geophys. Res. 110. https://doi.org/10.1029/2004JB003268.

Garg, D., Papale, P., Longo, A., 2021. A partitioned solver for compressible/incompressible fluid flow and light structure. Computers & Mathematics with Applications 100, 182–195. https://doi.org/10.1016/j.camwa.2021.09.005.

Gonnermann, H.M., Anderson, K., 2021. Modeling Volcano-Magmatic Systems: Workshop Report for the Modeling Collaboratory for Subduction Research Coordination Network. https://doi.org/10.31223/X55G96.

Gonzalez-Santana, J., Wauthier, C., 2021. Unraveling long-term volcano flank instability at Pacaya Volcano, Guatemala, using satellite geodesy. Journal of Volcanology and Geothermal Research 410, 107147. https://doi.org/10.1016/j.jvolgeores.2020.107147.

Grapenthin, R., Cheng, Y., Angarita, M., Tan, D., Meyer, F.J., Fee, D., Wech, A., 2022. Return from dormancy: rapid inflation and seismic unrest driven by transcrustal magma transfer at mt. edgecumbe (l'úx shaa) volcano, alaska. Geophys. Res. Lett. 49. https://doi.org/10.1029/2022GL099464.

Gregg, P.M., de Silva, S.L., Grosfils, E.B., 2013. Thermomechanics of shallow magma chamber pressurization: Implications for the assessment of ground deformation data at active volcanoes. Earth and Planetary Science Letters 384, 100–108. https://doi.org/10.1016/j.epsl.2013.09.040.

Harris, R.A., Barall, M., Aagaard, B., Ma, S., Roten, D., Olsen, K., Duan, B., Liu, D., Luo, B., Bai, K., Ampuero, J., Kaneko, Y., Gabriel, A., Duru, K., Ulrich, T., Wollherr, S., Shi, Z., Dunham, E., Bydlon, S., Zhang, Z., Dalguer, L., 2018. A suite of exercises for verifying dynamic earthquake rupture codes. Seismological Research Letters 89, 1146–1162. https://doi.org/10.1785/0220170222.

Harris, R.A., Barall, M., Andrews, D.J., Duan, B., Ma, S., Dunham, E.M., Gabriel, A.A., Kaneko, Y., Kase, Y., Aagaard, B.T., Oglesby, D.D., Ampuero, J.P., Hanks, T.C., Abrahamson, N., 2011. Verifying a computational method for predicting extreme ground motion. Seismological Research Letters 82, 638–644. https://doi.org/10.1785/gssrl.82.5.638.

Harris, R.A., Barall, M., Archuleta, R., Dunham, E., Aagaard, B., Ampuero, J.P., Bhat, H., Cruz-Atienza, V., Dalguer, L., Dawson, P., Day, S., Duan, B., Ely, G., Kaneko, Y., Kase, Y., Lapusta, N., Liu, Y., Ma, S., Oglesby, D., Olsen, K., Templeton, E., 2009. The SCEC/USGS dynamic earthquake rupture code verification exercise. Seismological Research Letters 80, 119–126. https://doi.org/10.1785/gssrl.80.1.119.

Hickey, J., Gottsmann, J., Nakamichi, H., Iguchi, M., 2016. Thermomechanical controls on magma supply and volcanic deformation: application to Aira caldera, Japan. Sci. Rep. 6, 32691. https://doi.org/10.1038/srep32691.

Hickey, J., Gottsmann, J., 2014. Benchmarking and developing numerical Finite Element models of volcanic deformation. Journal of Volcanology and Geothermal Research 280, 126–130. https://doi.org/10.1016/j.jvolgeores.2014.05.011.

Jiang, J., Erickson, B.A., Lambert, V.R., Ampuero, J., Ando, R., Barbot, S.D., Cattania, C., Zilio, L.D., Duan, B., Dunham, E.M., Gabriel, A., Lapusta, N., Li, D., Li, M., Liu, D., Liu, Y., Ozawa, S., Pranger,

C., van Dinther, Y., 2022. Community- driven code comparisons for three- dimensional dynamic modeling of sequences of earthquakes and aseismic slip. J. Geophys. Res. Solid Earth 127. https://doi.org/10.1029/2021JB023519.
Jonsson, S., 2002. Fault Slip Distribution of the 1999 Mw 7.1 Hector Mine, California, Earthquake, Estimated from Satellite Radar and GPS Measurements. Bulletin of the Seismological Society of America 92, 1377–1389. https://doi.org/10.1785/0120000922.
Karlstrom, L., Dufek, J., Manga, M., 2009. Organization of volcanic plumbing through magmatic lensing by magma chambers and volcanic loads. J. Geophys. Res. 114. https://doi.org/10.1029/2009JB006339.
Lindsay, A.D., Gaston, D.R., Permann, C.J., Miller, J.M., Andrš, D., Slaughter, A.E., Kong, F., Hansel, J., Carlsen, R.W., Icenhour, C., Harbour, L., Giudicelli, G.L., Stogner, R.H., German, P., Badger, J., Biswas, S., Chapuis, L., Green, C., Hales, J., Hu, T., Wong, C., 2022. 2.0 - MOOSE: Enabling massively parallel multiphysics simulation. SoftwareX 20, 101202. https://doi.org/10.1016/j.softx.2022.101202.
Lisowski, M., 2006. Analytical volcano deformation source models, in: Volcano Deformation. Springer Berlin Heidelberg, Berlin, Heidelberg, pp. 279–304. https://doi.org/10.1007/978-3-540-49302-0_8.
Liu, Y., 2016. On the displacement discontinuity method and the boundary element method for solving 3-D crack problems. Eng. Fract. Mech. 164, 35–45. https://doi.org/10.1016/j.engfracmech.2016.07.009.
Longo, A., Papale, P., Vassalli, M., Saccorotti, G., Montagna, C.P., Cassioli, A., Giudice, S., Boschi, E., 2012. Magma convection and mixing dynamics as a source of Ultra-Long-Period oscillations. Bull. Volcanol. 74, 873–880. https://doi.org/10.1007/s00445-011-0570-0.
Mai, P.M., Schorlemmer, D., Page, M., Ampuero, J., Asano, K., Causse, M., Custodio, S., Fan, W., Festa, G., Galis, M., Gallovic, F., Imperatori, W., Käser, M., Malytskyy, D., Okuwaki, R., Pollitz, F., Passone, L., Razafindrakoto, H.N.T., Sekiguchi, H., Song, S.G., Zielke, O., 2016. The earthquake- source inversion validation (SIV) project. Seismological Research Letters 87, 690–708. https://doi.org/10.1785/0220150231.
Masterlark, T., 2007. Magma intrusion and deformation predictions: Sensitivities to the Mogi assumptions. J. Geophys. Res. 112. https://doi.org/10.1029/2006JB004860.
McTigue, D.F., Segall, P., 1988. Displacements and tilts from dip-slip faults and magma chambers beneath irregular surface topography. Geophys. Res. Lett. 15, 601–604. https://doi.org/10.1029/GL015i006p00601.
McTigue, D.F., 1987. Elastic stress and deformation near a finite spherical magma body: Resolution of the point source paradox. J. Geophys. Res. 92, 12931. https://doi.org/10.1029/JB092iB12p12931.
Menke, W., 2018. Geophysical Data Analysis: Discrete Inverse Theory, 4th ed. Academic Press.
Mogi, K., 1958. Relation between the eruptions of various volcanoes and deformations of the ground surfaces around them. Bulletin of the Earthquake Research Institute 36, 99–134.
Montgomery-Brown, E.K., Karlstrom, L., Crozier, J.A., Bato, M.G., Cayol, V., Angarita, M., Grapenthin, R., Astort, A., Cannavo, F., Silverii, F., Others, 2022. Drivers of Volcano Deformation (DVD) Verification and Validation Exercises: Phase 1., in: AGU Fall Meeting. Presented at the AGU 2022 Fall Meeting, AGU, pp. V52D-0021.
Montgomery-Brown, E.K., Miklius, A., 2021. Periodic dike intrusions at Kīlauea volcano, Hawai'i. Geology 49, 397–401. https://doi.org/10.1130/G47970.1.
Mullet, B., Segall, P., 2022. The surface deformation signature of a transcrustal, crystal mush- dominant magma system. J. Geophys. Res. Solid Earth 127. https://doi.org/10.1029/2022JB024178.
Nikkhoo, M., Rivalta, E., 2022. Surface deformations and gravity changes caused by pressurized finite ellipsoidal cavities. Geophys. J. Int. 232, 643–655. https://doi.org/10.1093/gji/ggac351.
Nikkhoo, M., Walter, T.R., Lundgren, P.R., Prats-Iraola, P., 2017. Compound dislocation models (CDMs) for volcano deformation analyses. Geophys. J. Int. 208, 877–894. https://doi.org/10.1093/gji/ggw427.
Nikkhoo, M., Walter, T.R., 2015. Triangular dislocation: an analytical, artefact-free solution. Geophys. J.

Int. 201, 1119–1141. https://doi.org/10.1093/gji/ggv035.
Novoa, C., Remy, D., Gerbault, M., Baez, J.C., Tassara, A., Cordova, L., Cardona, C., Granger, M., Bonvalot, S., Delgado, F., 2019. Viscoelastic relaxation: A mechanism to explain the decennial large surface displacements at the Laguna del Maule silicic volcanic complex. Earth and Planetary Science Letters 521, 46–59. https://doi.org/10.1016/j.epsl.2019.06.005.
Parks, M.M., Biggs, J., England, P., Mather, T.A., Nomikou, P., Palamartchouk, K., Papanikolaou, X., Paradissis, D., Parsons, B., Pyle, D.M., Raptakis, C., Zacharis, V., 2012. Evolution of Santorini Volcano dominated by episodic and rapid fluxes of melt from depth. Nature Geosci. 5, 749–754. https://doi.org/10.1038/ngeo1562.
Poland, M.P., Peltier, A., Bonforte, A., Puglisi, G., 2017. The spectrum of persistent volcanic flank instability: A review and proposed framework based on Kīlauea, Piton de la Fournaise, and Etna. Journal of Volcanology and Geothermal Research 339, 63–80. https://doi.org/10.1016/j.jvolgeores.2017.05.004.
Poland, M.P., Zebker, H.A., 2022. Volcano geodesy using InSAR in 2020: the past and next decades. Bull. Volcanol. 84, 27. https://doi.org/10.1007/s00445-022-01531-1.
Rucker, C., Erickson, B.A., Karlstrom, L., Lee, B., Gopalakrishnan, J., 2022. A computational framework for time- dependent deformation in viscoelastic magmatic systems. J. Geophys. Res. Solid Earth 127. https://doi.org/10.1029/2022JB024506.
Sahagian, D., 2005. Volcanic eruption mechanisms: Insights from intercomparison of models of conduit processes. Journal of Volcanology and Geothermal Research 143, 1–15. https://doi.org/10.1016/j.jvolgeores.2004.12.006.
Segall, P., 2019. Magma chambers: what we can, and cannot, learn from volcano geodesy. Philos. Transact. A Math. Phys. Eng. Sci. 377, 20180158. https://doi.org/10.1098/rsta.2018.0158.
Segall, P., 2010. Earthquake and volcano deformation. Princeton University Press, Princeton. https://doi.org/10.1515/9781400833856.
Sigmundsson, F., Hooper, A., Hreinsdóttir, S., Vogfjörd, K.S., Ófeigsson, B.G., Heimisson, E.R., Dumont, S., Parks, M., Spaans, K., Gudmundsson, G.B., Drouin, V., Árnadóttir, T., Jónsdóttir, K., Gudmundsson, M.T., Högnadóttir, T., Fridriksdóttir, H.M., Hensch, M., Einarsson, P., Magnússon, E., Samsonov, S., Eibl, E.P.S., 2015. Segmented lateral dyke growth in a rifting event at Bárðarbunga volcanic system, Iceland. Nature 517, 191–195. https://doi.org/10.1038/nature14111.
Sigmundsson, F., Pinel, V., Grapenthin, R., Hooper, A., Halldórsson, S.A., Einarsson, P., Ófeigsson, B.G., Heimisson, E.R., Jónsdóttir, K., Gudmundsson, M.T., Vogfjörd, K., Parks, M., Li, S., Drouin, V., Geirsson, H., Dumont, S., Fridriksdottir, H.M., Gudmundsson, G.B., Wright, T.J., Yamasaki, T., 2020. Unexpected large eruptions from buoyant magma bodies within viscoelastic crust. Nat. Commun. 11, 2403. https://doi.org/10.1038/s41467-020-16054-6.
Tarantola, A., 2004. Inverse Problem Theory and Methods for Model Parameter Estimation, 1st ed. SIAM: Society for Industrial and Applied Mathematics, Philadelphia, PA.
Taylor, N.C., Johnson, J.H., Herd, R.A., 2021. Making the most of the Mogi model: Size matters. Journal of Volcanology and Geothermal Research 419, 107380. https://doi.org/10.1016/j.jvolgeores.2021.107380.
Townsend, M., 2022. Linking surface deformation to thermal and mechanical magma chamber processes. Earth and Planetary Science Letters 577, 117272. https://doi.org/10.1016/j.epsl.2021.117272.
Trasatti, E., 2022. Volcanic and seismic source modeling: an open tool for geodetic data modeling. Front. Earth Sci. 10. https://doi.org/10.3389/feart.2022.917222.
Williams, C.A., Wadge, G., 2000. An accurate and efficient method for including the effects of topography in three-dimensional elastic models of ground deformation with applications to radar interferometry. J. Geophys. Res. 105, 8103–8120. https://doi.org/10.1029/1999JB900307.
Williams, C.A., Wadge, G., 1998. The effects of topography on magma chamber deformation models:

Application to Mt. Etna and radar interferometry. Geophys. Res. Lett. 25, 1549–1552. https://doi.org/10.1029/98GL01136.
Yang, X.-M., Davis, P.M., Dieterich, J.H., 1988. Deformation from inflation of a dipping finite prolate spheroid in an elastic half-space as a model for volcanic stressing. J. Geophys. Res. 93, 4249–4257. https://doi.org/10.1029/JB093iB05p04249.
Zhong, X., Dabrowski, M., Jamtveit, B., 2019. Analytical solution for the stress field in elastic half-space with a spherical pressurized cavity or inclusion containing eigenstrain. Geophys. J. Int. 216, 1100–1115. https://doi.org/10.1093/gji/ggy447.
Zienkiewicz, O.C., 2005. The Finite Element Method: Its Basis and Fundamentals, 6th ed. Butterworth-Heinemann.

Supplementary Information for:

Understanding the drivers of volcano deformation through geodetic model verification and validation

Josh Crozier, Leif Karlstrom, Emily Montgomery-Brown, Mario Angarita, Valérie Cayol, Mary Grace Bato, Taiyi A. Wang, Ronni Grapenthin, Tara Shreve, Kyle Anderson, Ana Astort, Olivier Bodart, Flavio Cannavò, Gilda Currenti, Farshid Dabaghi, Brittany A. Erickson, Deepak Garg, Matthew Head, Adriana Iozzia, Young Cheol Kim, Hélène Le Mével, Camila Novoa Lizama, Cody Rucker, Francesca Silverii, Elisa Trasatti, Yan Zhan

Contents: Supplemental figures S1-S12.

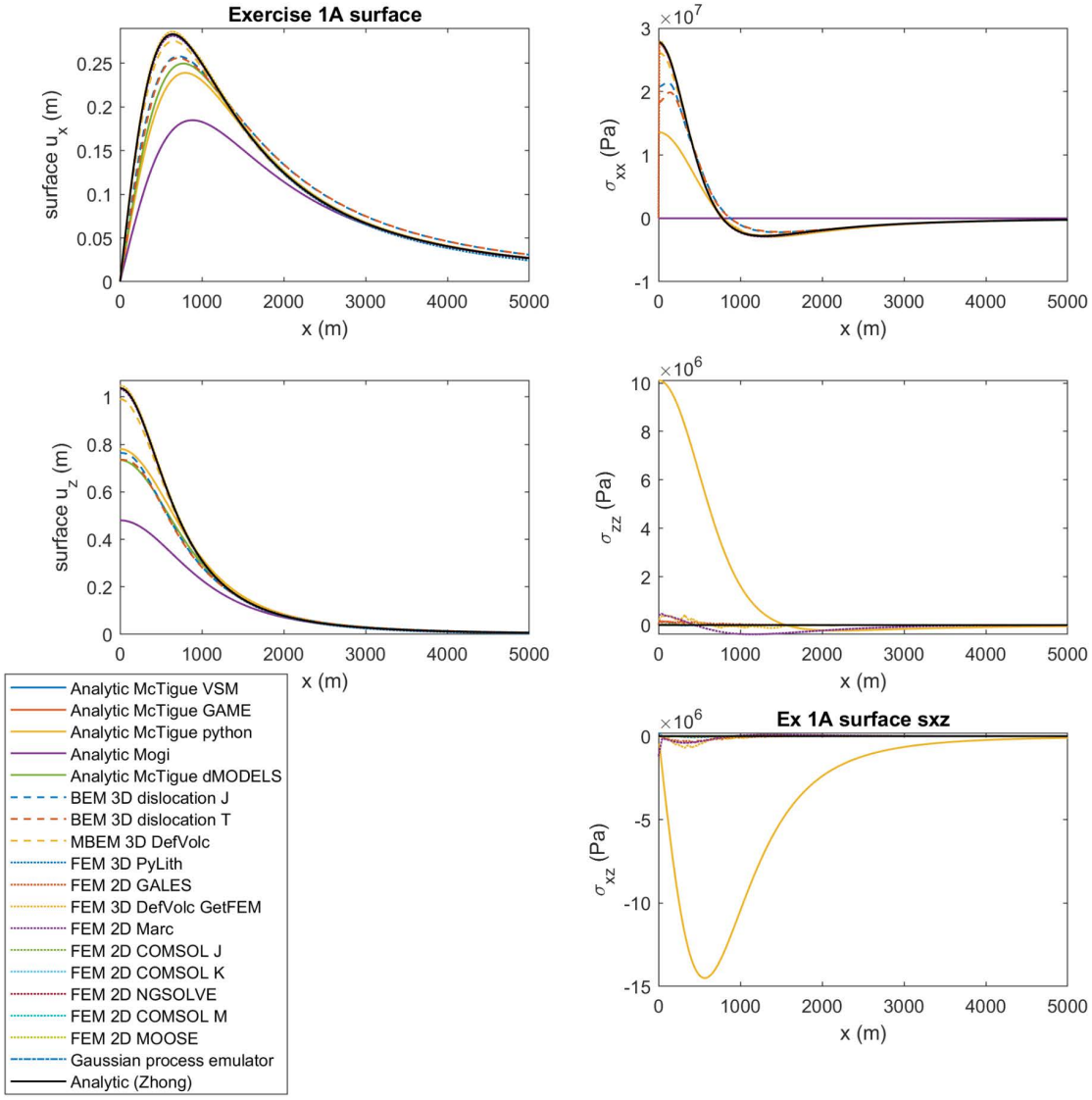

Figure S1. Exercise 1A displacements and stresses at the ground surface.

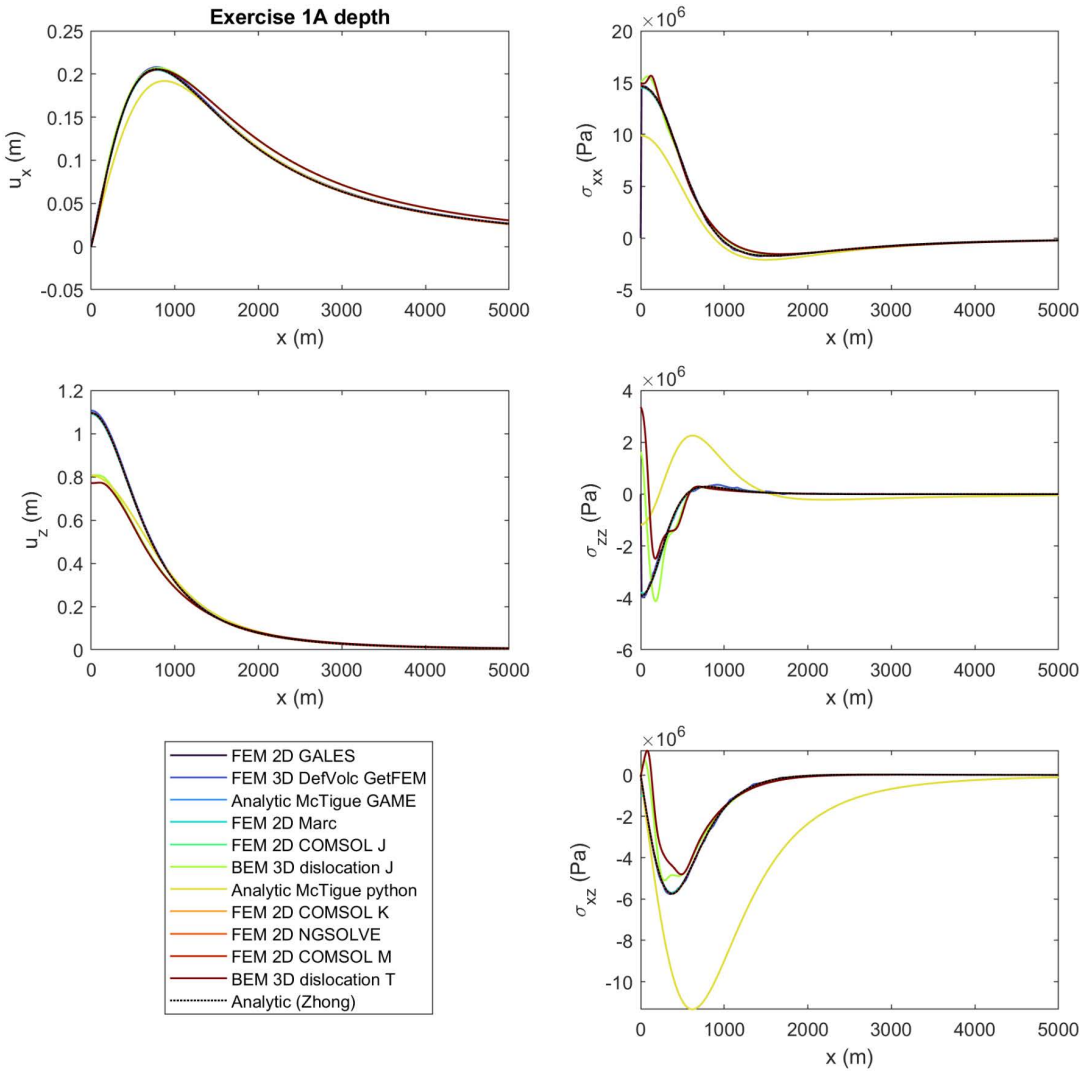

Figure S2. Exercise 1A displacements and stresses at depth.

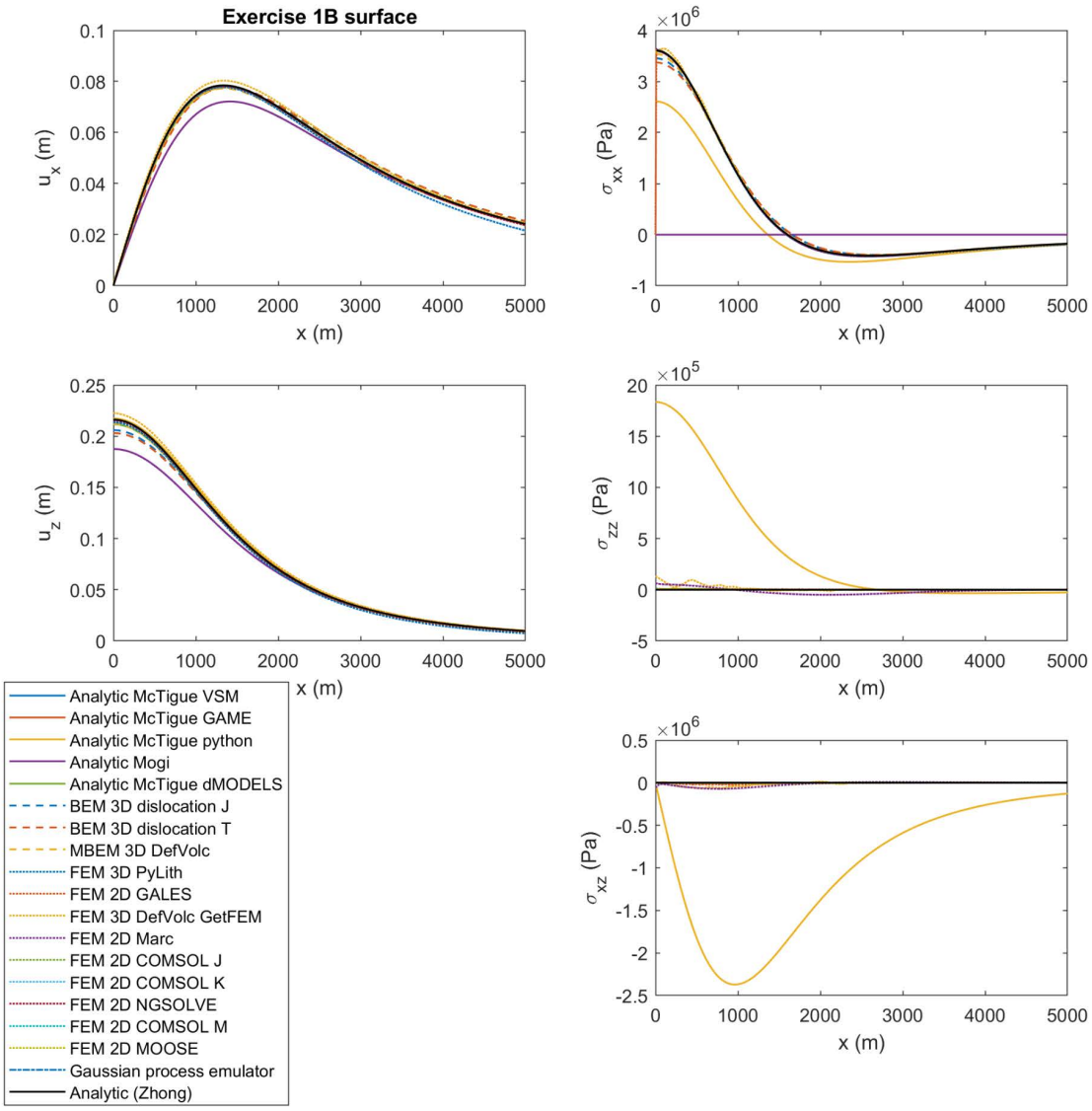

Figure S3. Exercise 1B displacements and stresses at the ground surface.

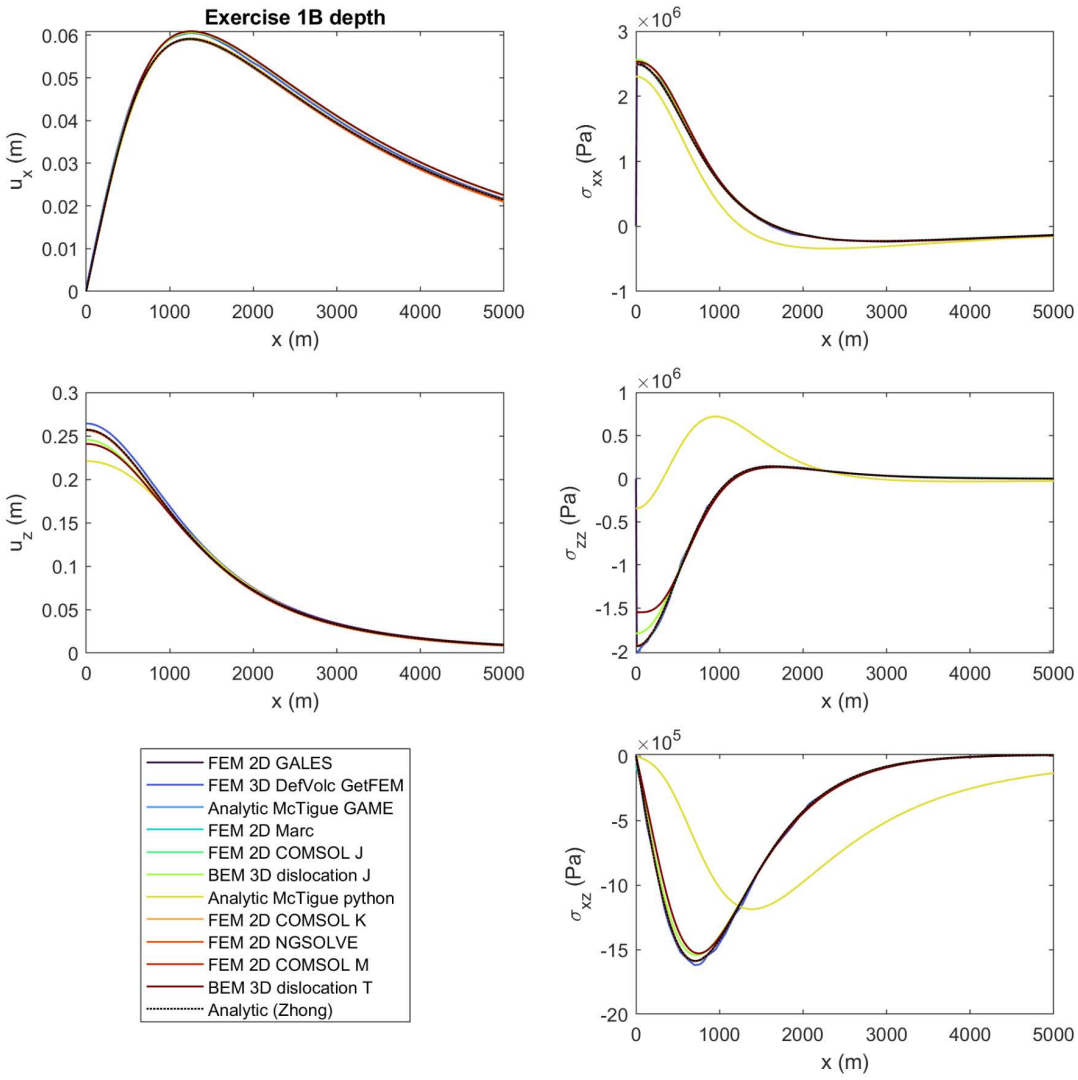

Figure S4. Exercise 1B displacements and stresses at depth.

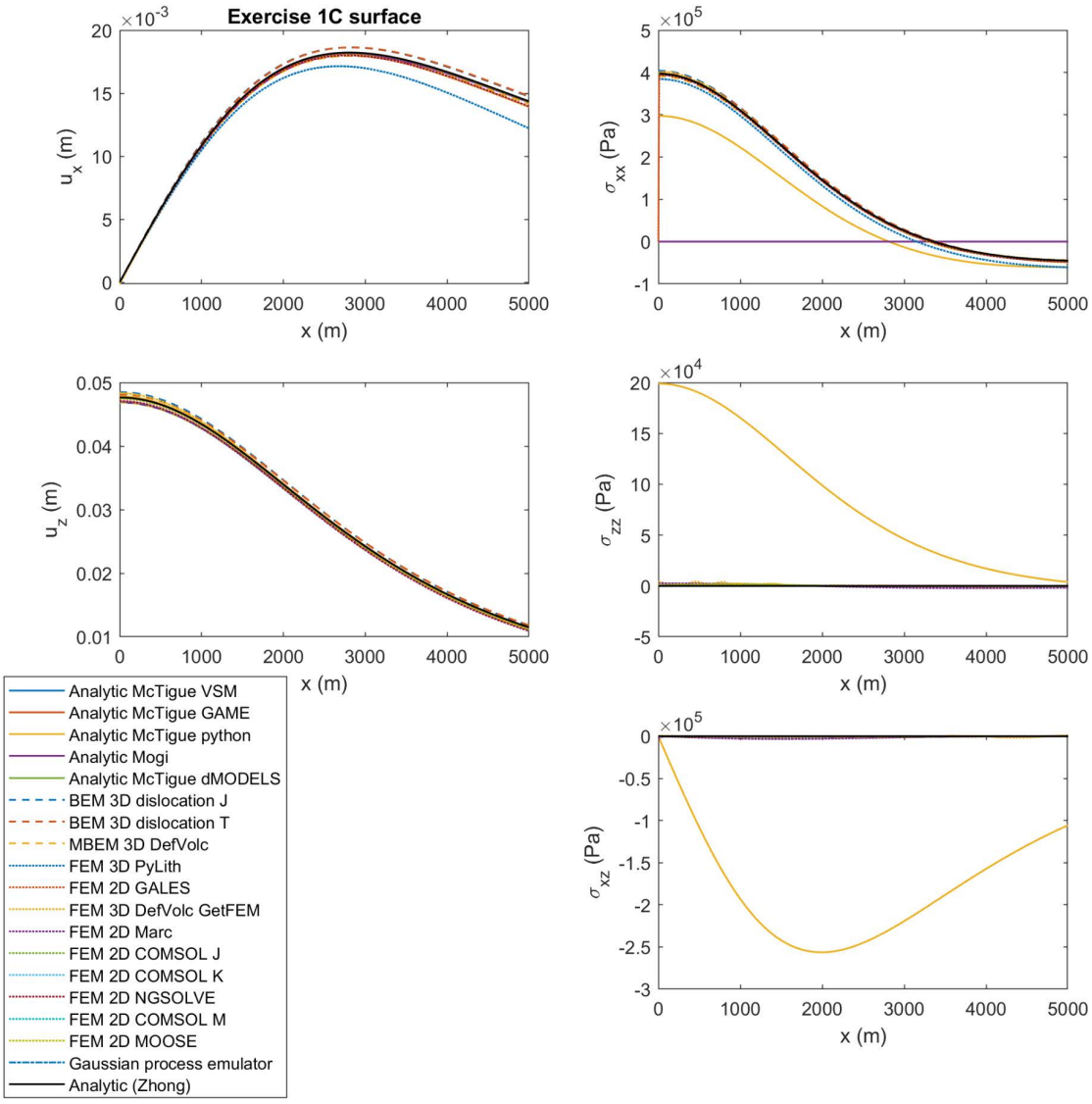

Figure S5. Exercise 1C displacements and stresses at the ground surface.

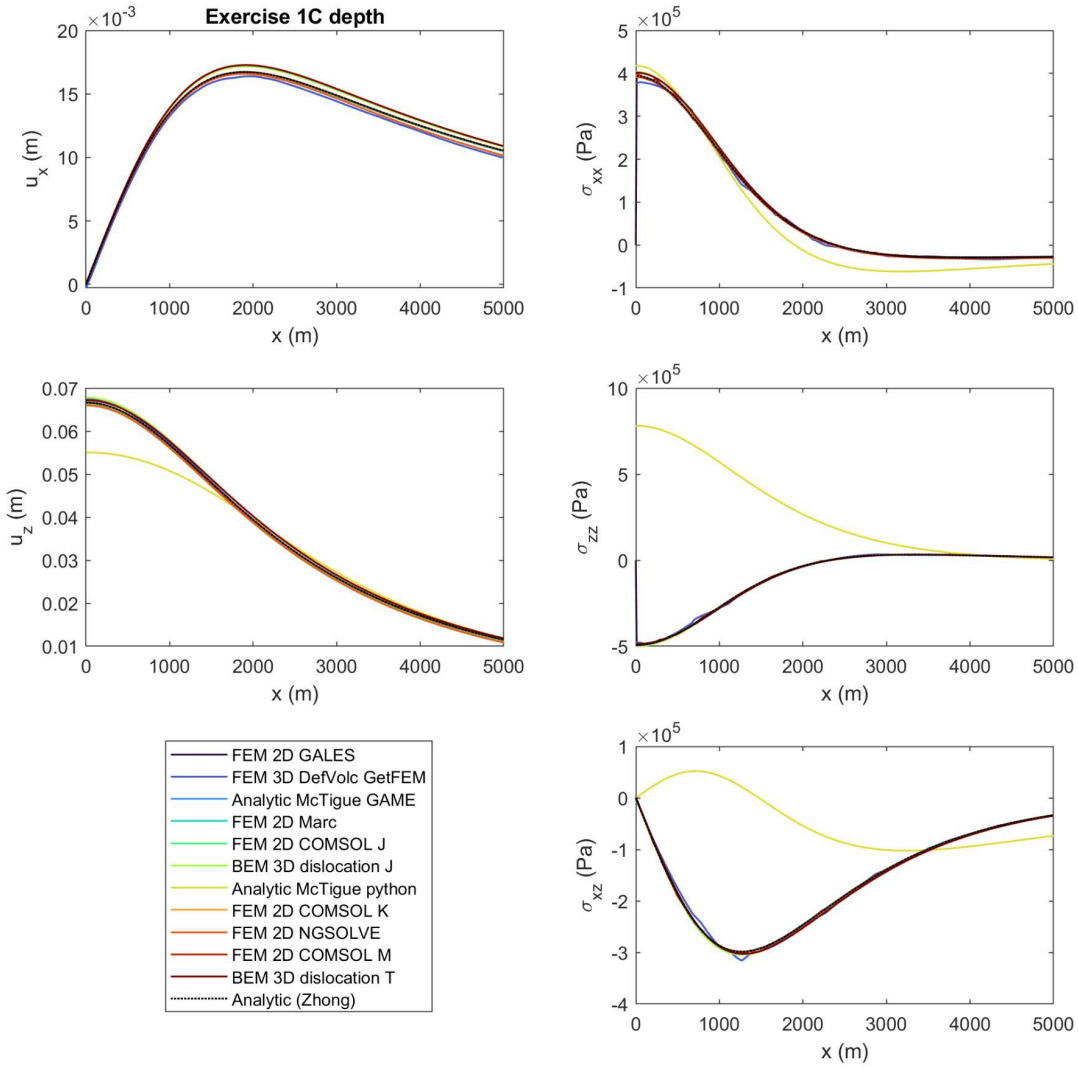

Figure S6. Exercise 1C displacements and stresses at depth.

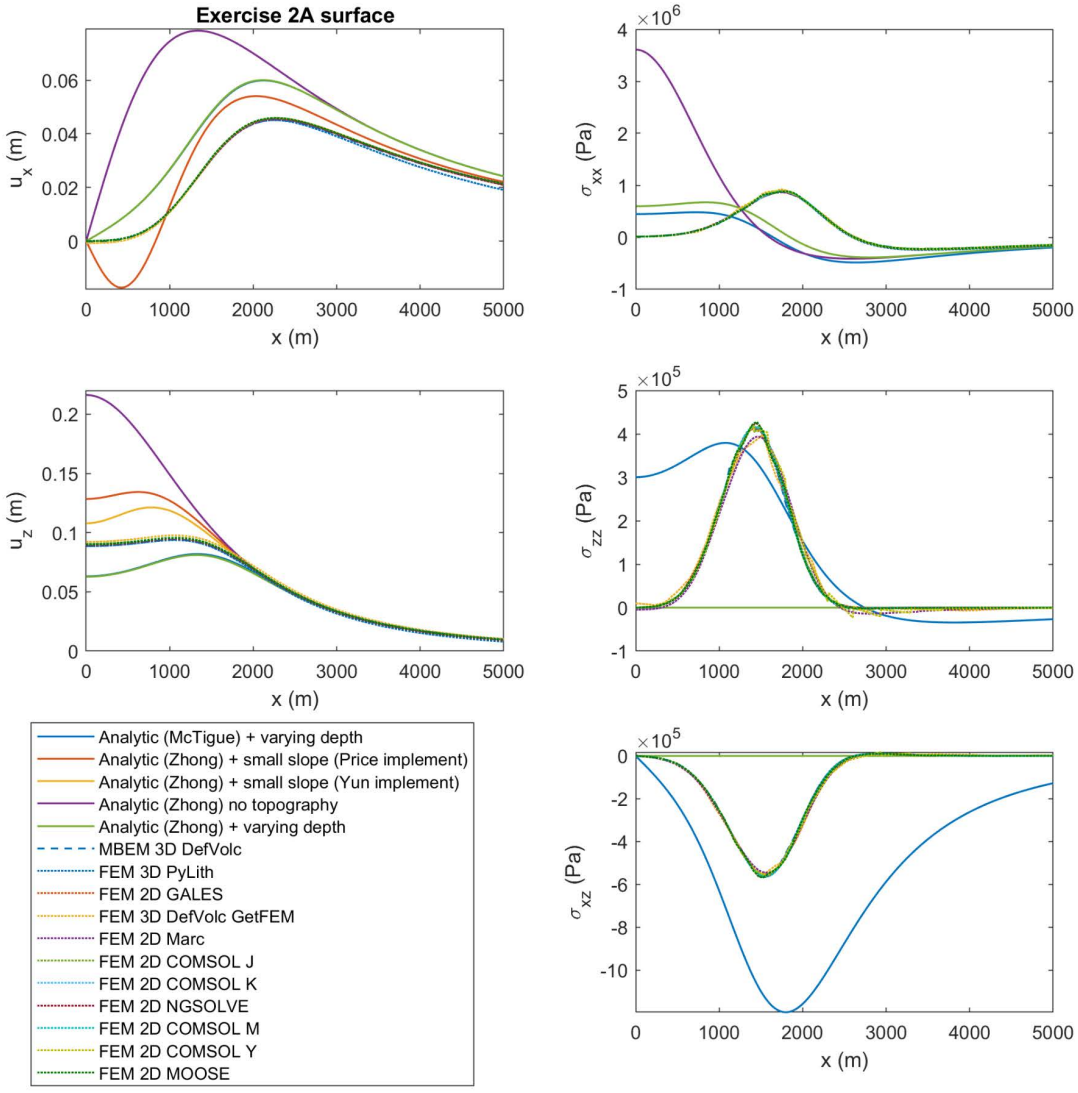

Figure S7. Exercise 2A displacements and stresses at the ground surface.

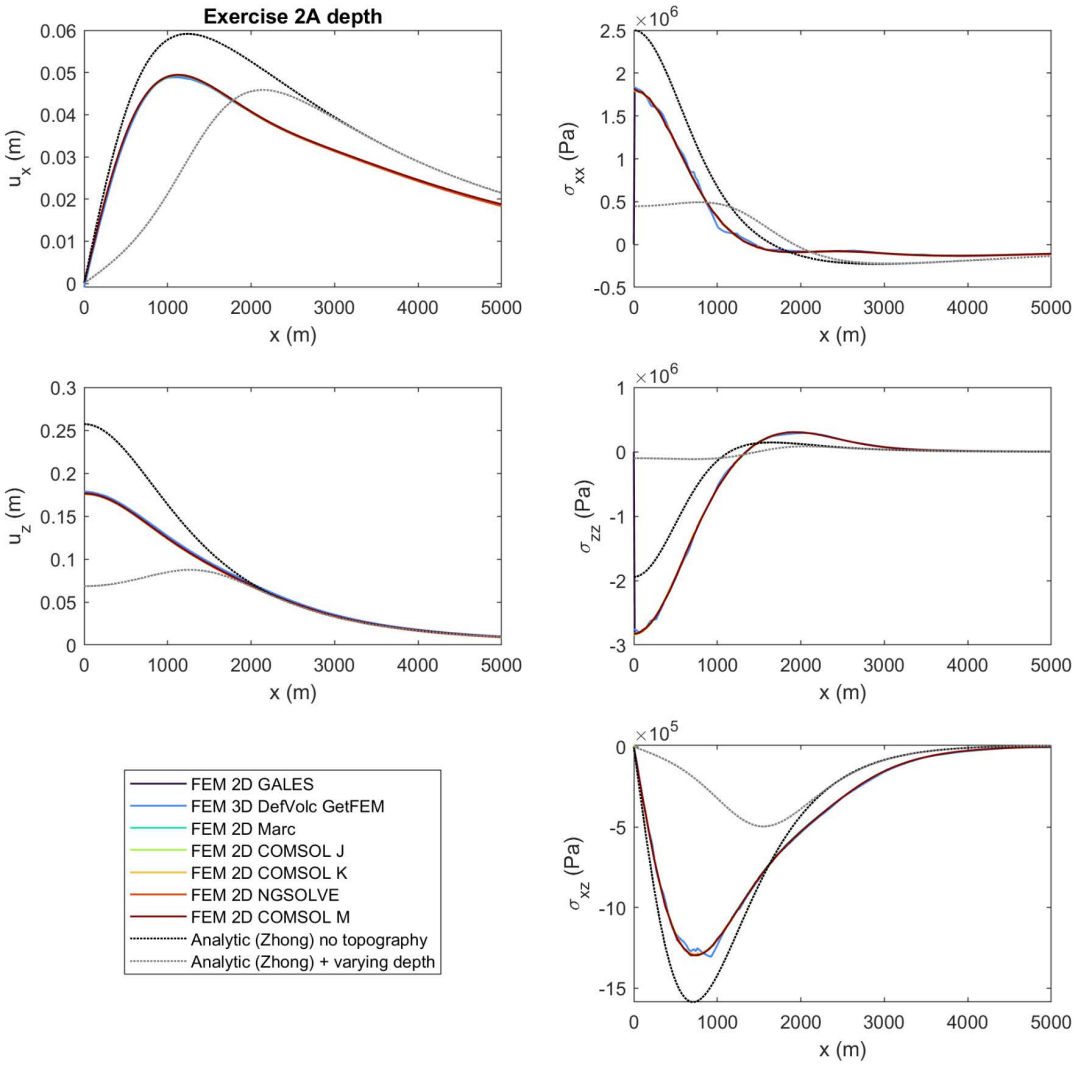

Figure S8. Exercise 2A displacements and stresses at depth.

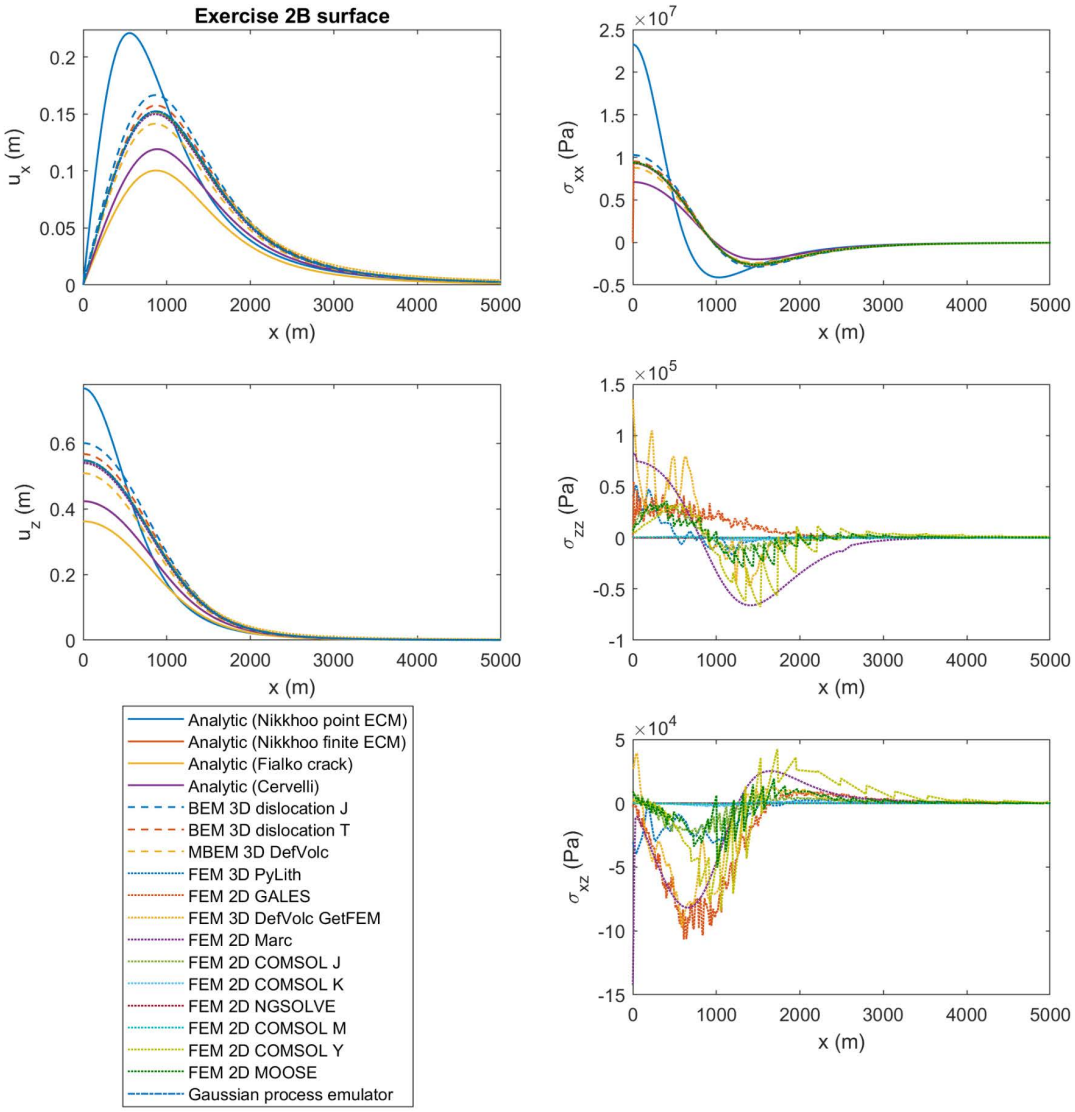

Figure S9. Exercise 2B displacements and stresses at the ground surface.

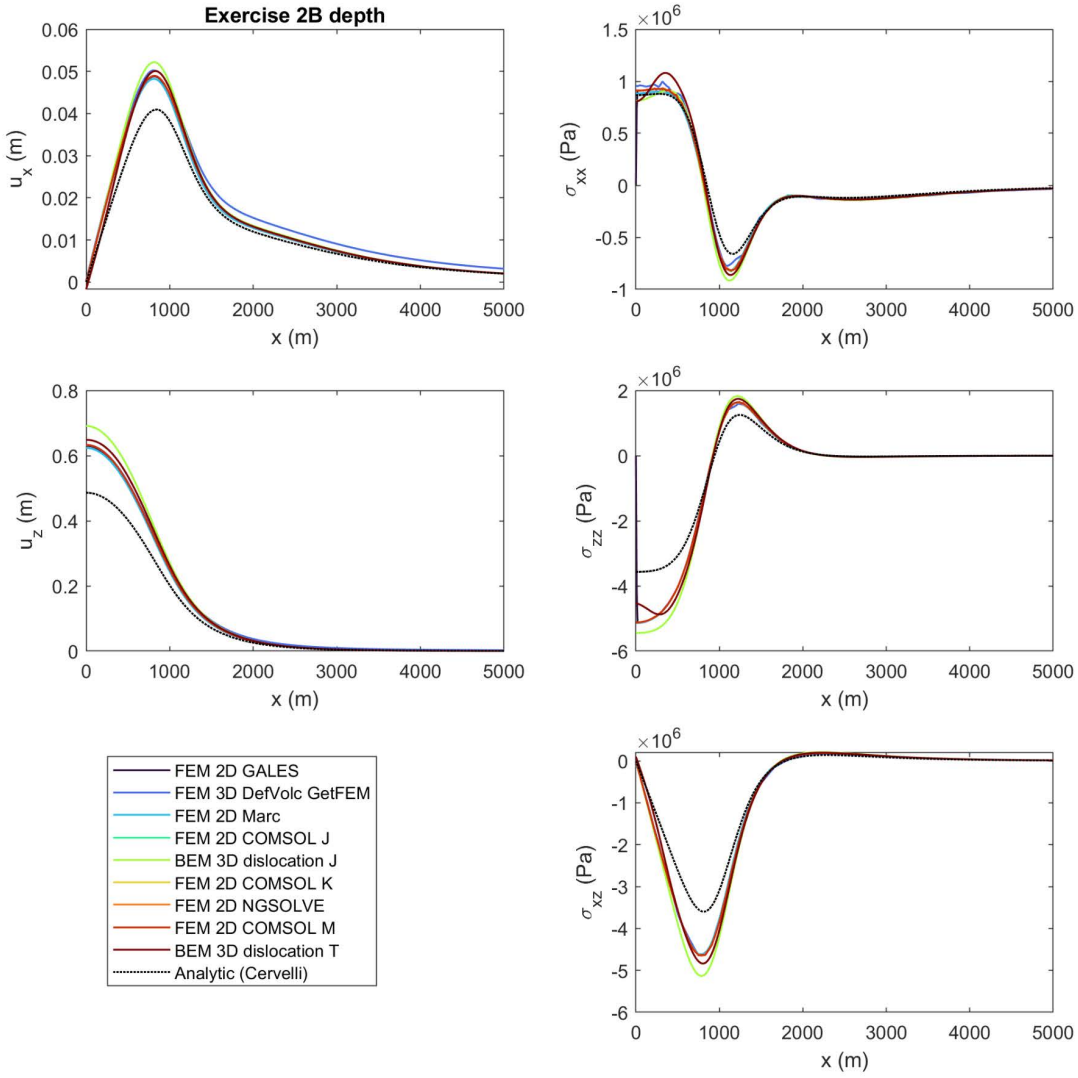

Figure S10. Exercise 2B displacements and stresses at depth.

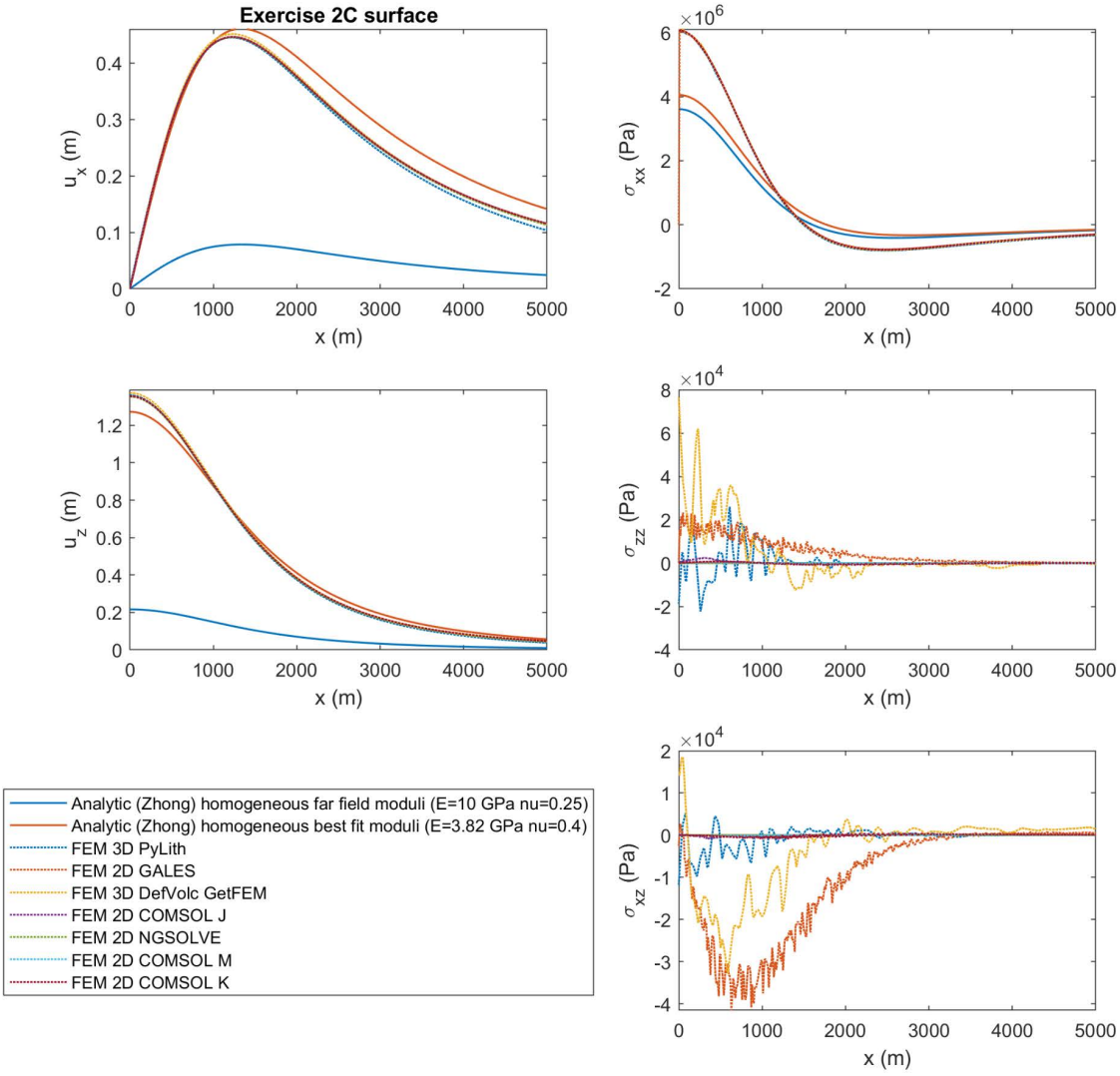

Figure S11. Exercise 2C displacements and stresses at the ground surface.

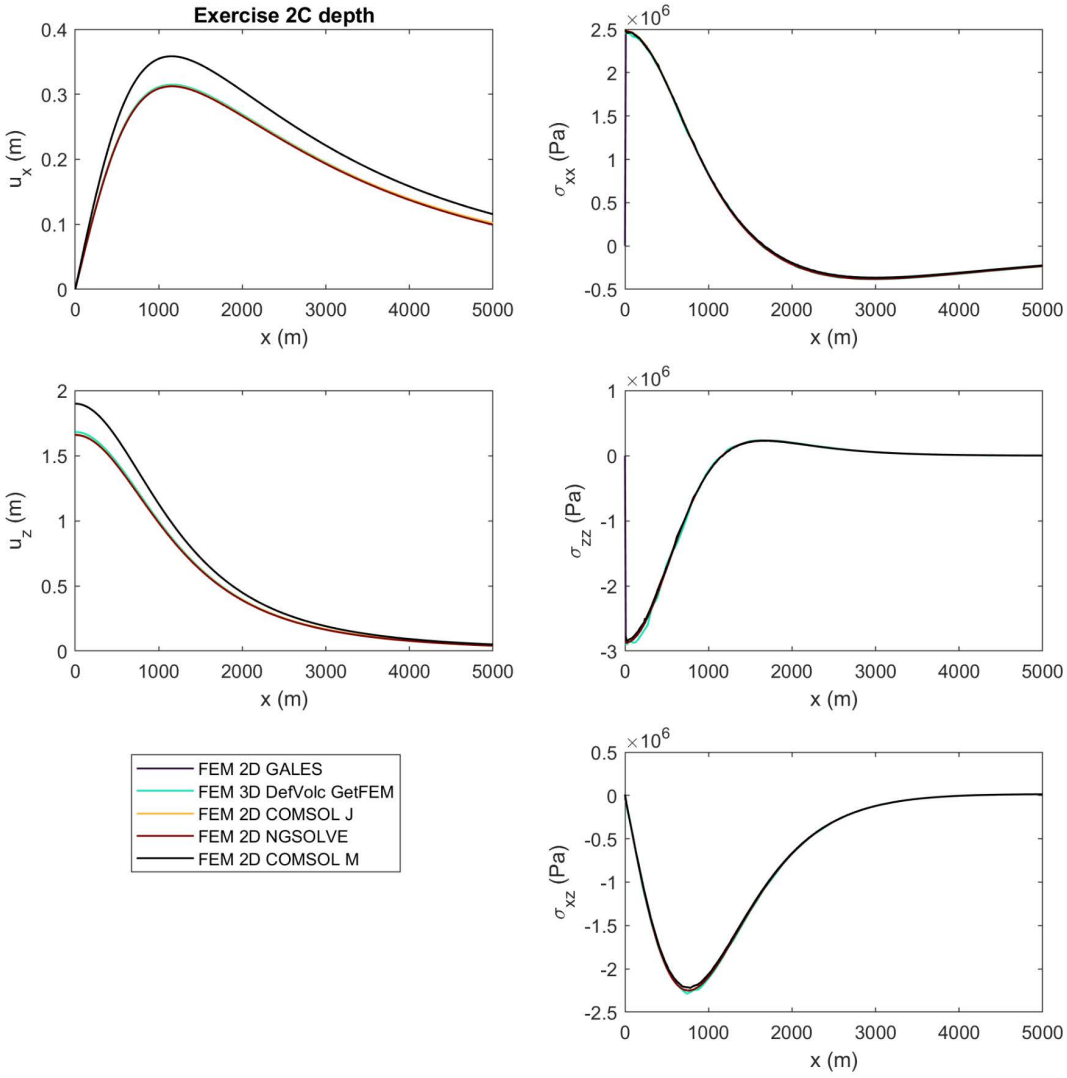

Figure S12. Exercise 2C displacements and stresses at depth.